





A neuropathy-associated kinesin KIF1A mutation hyper-stabilizes the motor-neck interaction during the ATPase cycle

Manatsu Morikawa¹, Nivedita U Jerath^{2,3}, Tadayuki Ogawa^{1,4} , Momo Morikawa^{1,5} ,
Yosuke Tanaka¹ , Michael E Shy², Stephan Zuchner⁶ & Nobutaka Hirokawa^{1,*} 

Abstract

The mechanochemical coupling of ATPase hydrolysis and conformational dynamics in kinesin motors facilitates intramolecular interaction cycles between the kinesin motor and neck domains, which are essential for microtubule-based motility. Here, we characterized a charge-inverting KIF1A-E239K mutant that we identified in a family with axonal-type Charcot-Marie-Tooth disease and also in 24 cases in human neuropathies including spastic paraplegia and hereditary sensory and autonomic neuropathy. We show that Glu239 in the $\beta 7$ strand is a key residue of the motor domain that regulates the motor-neck interaction. Expression of the KIF1A-E239K mutation has decreased ability to complement *Kif1a*^{+/-} neurons, and significantly decreases ATPase activity and microtubule gliding velocity. X-ray crystallography shows that this mutation causes an excess positive charge on $\beta 7$, which may electrostatically interact with a negative charge on the neck. Quantitative mass spectrometric analysis supports that the mutation hyper-stabilizes the motor-neck interaction at the late ATP hydrolysis stage. Thus, the negative charge of Glu239 dynamically regulates the kinesin motor-neck interaction, promoting release of the neck from the motor domain upon ATP hydrolysis.

Keywords axonal transport; human neuropathies; KIF1A; motor-neck interaction; neuropathy-related mutation

Subject Categories Cell Adhesion, Polarity & Cytoskeleton; Neuroscience

DOI 10.15252/emboj.2021108899 | Received 7 June 2021 | Revised 21 December 2021 | Accepted 22 December 2021 | Published online 8 February 2022

The EMBO Journal (2022) 41: e108899

Introduction

Kinesin superfamily proteins (KIFs) are a class of motor proteins that are involved in essential biological processes, including

intracellular transport, the organization of spindle microtubules, and chromosome segregation. In neurons, KIFs are responsible for long-distance transport between cell bodies, axons, and dendrites and are important for maintaining neuronal function and morphology (Hirokawa, 1998). More than 45 *KIF* genes have been identified in mammalian genomes, and they are classified into 15 families (Miki *et al*, 2001; Lawrence *et al*, 2004). Each KIF binds to specific cargoes, including membrane organelles and supramolecular complexes, via adapter proteins and transports them to their destinations along microtubules using energy from ATP hydrolysis (Hirokawa *et al*, 2009a, 2009b). How the mechanochemical ATPase cycle of the KIF motor is maintained by inter- and intramolecular interactions is an important topic in intracellular transport.

KIF1A is a member of the kinesin-3 family. It transports synaptic vesicle precursors and TrkA-containing vesicles from the cell body to the axon tip (Hall & Hedgecock, 1991; Okada *et al*, 1995; Tanaka *et al*, 2016). *Kif1a*^{-/-} mice die shortly after birth with reduced density of synaptic vesicles at the nerve endings and vesicle accumulation in the neuronal cell body (Yonekawa *et al*, 1998). In mouse dorsal root ganglion (DRG) neurons, KIF1A transports TrkA, an essential driver of the PI3 kinase signaling pathway that facilitates the surface presentation of the capsaicin receptor TRPV1 channel. Therefore, KIF1A is involved in the development of pain; thus, *Kif1a*^{+/-} mice have a phenotype of progressive sensory impairment (Tanaka *et al*, 2016). According to these essential functions of KIF1A, gene mutations in *KIF1A* are closely associated with axonal neuropathy and various neurological symptoms in humans (Esmaeeli Nieh *et al*, 2015; Ohba *et al*, 2015; Cheon *et al*, 2017; Chiba *et al*, 2019). Charcot-Marie-Tooth disease (CMT) is one of the most common inherited peripheral neuropathies related with KIF1 family members (Zhao *et al*, 2001; Tanaka & Hirokawa, 2002; Xu *et al*, 2018). It is also called hereditary motor and sensory neuropathy (HMSN) and particularly affects peripheral nerves (Bucci *et al*, 2012). CMT progresses from the lower extremities to the forearms, with loss of sensation in the toes, fingers, and extremities. The

1 Department of Cell Biology and Anatomy, Graduate School of Medicine, The University of Tokyo, Tokyo, Japan

2 Department of Neurology, Carver College of Medicine, University of Iowa, Iowa City, IA, USA

3 Neuromuscular Division, AdventHealth Orlando, Winter Park, FL, USA

4 Research Center for Advanced Medical Science, Dokkyo Medical University, Mibu, Japan

5 Department of Anatomy and Neuroscience, Faculty of Medicine, University of Tsukuba, Tsukuba, Japan

6 Department of Human Genetics and Hussman Institute for Human Genomics, Miller School of Medicine, University of Miami, Miami, FL, USA

*Corresponding author. Tel: +81 3 5841 3326; E-mail: hirokawa@m.u-tokyo.ac.jp

prevalence is estimated to be 1/2,500 (Skre, 1974), with approximately 2.6 million patients worldwide (Ben Othmane *et al.*, 1993). Although more than 80 types of genes responsible for CMT have been identified, the full picture of the relationship between the genes and pathogenic mechanisms has yet to be elucidated (Verhoeven *et al.*, 2006; Timmerman *et al.*, 2014; Ekins *et al.*, 2015). Hereditary spastic paraplegia-30 (SPG30) and hereditary sensory and autonomic neuropathy (HSN2C) are also neurodegenerative diseases associated with *KIF1A* gene. SPG30 is a slowly progressive spastic paraplegia, and patients exhibit unsteady spastic gait and hyperreflexia of the lower extremities (Pennings *et al.*, 2020). Some patients have additional neurological abnormalities such as learning disability, ataxia, and optic neuropathy (Klebe *et al.*, 2012; Ylikallio *et al.*, 2015; Roda *et al.*, 2017). HSN2C related with *KIF1A* variants begins with progressive distal sensory loss, leading to ulceration and amputation of the fingers and toes (Rivire *et al.*, 2011). Patients have distal muscle weakness that primarily affects the lower extremities, and additional features including low IQ and slowed speech development.

Molecular structural studies of *KIF1A* have provided a better understanding of intramolecular coordination throughout the mechanochemical ATPase cycle. The *KIF1A* protein contains a motor domain and a neck domain (including a neck-linker and neck-coil) at the N-terminus (Fig 1B) (Hua *et al.*, 1997; Schnitzer & Block, 1997; Wordeman, 2003). The motor domain is a force-producing catalytic core that contains nucleotide-binding regions and microtubule-binding regions on both sides of the central β -sheet. ATP hydrolysis in nucleotide-binding regions affects the conformation of microtubule-binding regions and induces unbinding and binding to microtubules (Sindelar & Downing, 2010; Cao *et al.*, 2014). Thus, kinesin recognizes an appropriate position on microtubules in an ATP-dependent manner (Yajima *et al.*, 2012; Morikawa *et al.*, 2015). The neck-linker, a short flexible peptide of 11 residues that follows from the motor domain, switches its interaction with the motor domain dynamically in response to the ATPase cycle, giving rise to a “docked conformation” in the ATP state and an “undocked conformation” in the ADP state (Rice *et al.*, 1999; Kikkawa *et al.*, 2001). Docking of the neck-linker to the motor domain is considered to be the major force generation step of kinesins (Case *et al.*, 2000; Sindelar *et al.*, 2002; Tomishige *et al.*, 2006). The switching of motor-neck interactions produces stalk rotation, alters motor affinity for nucleotides and microtubules (Tripet *et al.*, 1997; Liu *et al.*, 2012), and induces directional movement on microtubules (Endow & Higuchi, 2000; Yildiz *et al.*, 2008; Yamagishi *et al.*, 2016). Another key region, $\beta 7$, is one of the β -strands in the central β -sheet spanning between the surface and the center of the motor domain. The C-terminal side of $\beta 7$ is followed by the microtubule-binding loop L11 (switch II), which can communicate with the nucleotide-binding loop L9 (switch I) and has been reported to be important for kinesin motor activity (Woehlke *et al.*, 1997; Brendza *et al.*, 2000; Shimizu *et al.*, 2000; Klumpp *et al.*, 2003; Auerbach & Johnson, 2005; Uchimura *et al.*, 2010); however, the N-terminal side of $\beta 7$ is located at the plus-end tip and is not part of the nucleotide- or microtubule-binding region. According to the molecular structure of the KIF motor domain (Kikkawa *et al.*, 2001; Nitta *et al.*, 2004; Sindelar, 2011; Atherton *et al.*, 2014) and the molecular dynamics simulation (Hwang *et al.*, 2008; Scarabelli & Grant, 2013; Budaitis *et al.*, 2019),

the N-terminal side of $\beta 7$ is expected to interact with the neck domain, but it has been unclear whether this interaction is related to physiological motor activity and intracellular trafficking.

Here, by exome sequencing, we identified a missense mutation caused by a single-base substitution in the *KIF1A* gene in a family with the axonal form of CMT (CMT2). Genome database also shows the same variant in 24 cases of human neuropathies including SPG30 and HSN2C. This variant causes a charge reversal on the N-terminal side of the $\beta 7$ region within the motor domain of *KIF1A*. To investigate the effect of this $\beta 7$ mutation on the kinesin driving mechanism, we characterized the motor activity decrease of the *KIF1A*-E239K mutant protein using mouse DRG neurons and an *in vitro* motility assay. Structural comparisons by X-ray crystallography and the quantification of site-specific interactions by mass spectrometry provide evidence that $\beta 7$ interacts electrostatically with the neck domain during the docked conformation and that this interaction is abnormally prolonged in the mutant. Therefore, the charge reversal in Glu239 in $\beta 7$ may interfere with structural changes in the neck domain, leading to a delay in the ATPase cycle. These results suggest a new essential role of the $\beta 7$ strand as a regulator of the motor-neck interaction for the proper progression of the kinesin ATPase cycle. This will shed light on the relevance of the motor-neck interaction in kinesin velocity regulation, providing new insights into the pivotal role of this dynamic interdomain interaction in motor protein mechanics.

Results

A peripheral neuropathy pedigree with a *KIF1A* mutation

We identified a hereditary neuropathy pedigree (Fig 1A). The age of disease onset in two brothers was between 60 and 70 years of age (Table 1). They both had a CMT2 phenotype with slowly progressive atrophy, weakness, and mild sensory loss in distal limbs. They both struggled with bilateral steppage gait and balance difficulties. The clinical severity based on their CMTNSv2 was mild to moderate (Murphy *et al.*, 2011). The velocity of ulnar motor nerve conduction ranged from 45 to 50 m/s. Further clinical details are shown in Table 1.

To identify the genetic cause of disease in our subjects, we performed exome sequencing. As a result, we found a heterozygous variant in the *KIF1A* gene c.715G>A, p.Glu239Lys (p.E239K), in both affected brothers (Table 2). We did not find any responsible variants in already identified 102 genes related to CMT2 such as *MFN2* (Table 2). In total, the exome of the index patient carried 187 missense and insertion/deletion variants that had a minor allele frequency of less than 0.001 and a genotype quality > 125. Several control databases, such as EVS, 1000 Genomes, and the GENESIS database, did not show any additional individuals with this variant. GnomAD reports a low frequency of 0.00004 for this change. Importantly, given that this was a late onset neuropathy in both brothers, we considered this variant causative but potentially with reduced or variable penetrance in the population, thus explaining the observed minor allele frequency in controls. In addition, the ClinVar database shows the same variant in *KIF1A* gene in 24 SPG30 and HSN2C

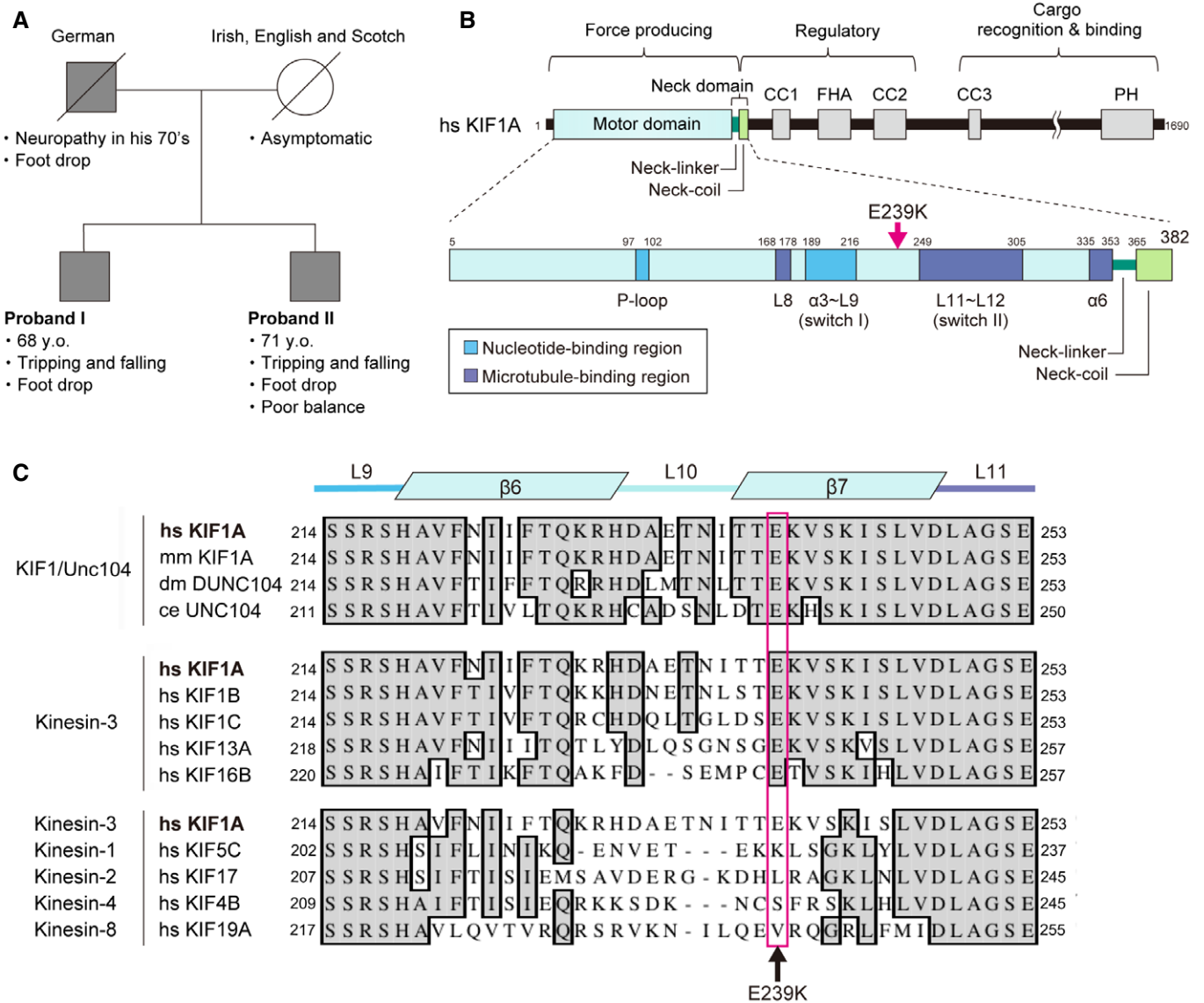


Figure 1. A neuropathy-related mutation identified in the KIF1A gene.

A Family pedigree of CMT2 patients. The probands I and II were genetically confirmed to carry the p.E239K variant in KIF1A. Their father also had foot drop symptoms and was clinically diagnosed with neuropathy in his 70s, while their mother was asymptomatic.

B Domain architecture of human KIF1A showing the position of the E239K mutation. KIF1A is composed of a motor domain, neck-linker, and neck-coil in the N-terminal force producing region, a regulatory domain in the middle, and a cargo recognition and binding domain in the C-terminal region.

C Multiple sequence alignment showing amino acids 214–253 of human KIF1A. E239 is located at β7 and is highly conserved in kinesin-3 members throughout evolution. hs, *Homo sapiens*; mm, *Mus musculus*; dm, *Drosophila melanogaster*; ce, *Caenorhabditis elegans*.

patients of human neuropathies (<https://www.ncbi.nlm.nih.gov/clinvar/RCV001211242.2/>).

The variant is located within the β7 strand in the motor domain of the KIF1A protein (Fig 1B and C). As shown by the sequence alignment, the residue is evolutionarily highly conserved across species and common in kinesin-3 family member proteins (KIF1B, KIF1C, KIF13A, and KIF16B) (Fig 1C). This amino acid is located in neither the microtubule-binding regions nor the nucleotide-binding regions where pathogenic missense KIF1A variants have been previously identified (Lee et al, 2015).

The KIF1A mutant was functionally impaired in its transport activity

To investigate how this mutant E239K affects the sensory nerves of patients, we examined the localization of the known KIF1A cargo proteins TrkA, Rab3A, synaptotagmin, and DENN/MADD (Hall & Hedgecock, 1991; Okada et al, 1995; Niwa et al, 2008; Tanaka et al, 2016). DRG neurons dissected from 9- to 12-month-old KIF1A WT (*Kif1a^{+/+}*) and heterozygous knockout (*Kif1a^{+/-}*) mice were transduced with KIF1A-EGFP and KIF1A(E239K)-EGFP

Table 1. Clinical phenotype of affected individuals carrying the p.E239K mutation in KIF1A.

	Subject I	Subject II
Age at study	68	71
Sex	M	M
Age at onset	61	70
Initial symptoms	Frequent tripping and falling, foot drop	Frequent tripping and falling, foot drop, and poor balance
Muscle atrophy UL	Yes, distal	Yes, distal
Muscle atrophy LL	Yes, distal	No
Muscle weakness UE	4- (thumb abduction) 4 (first dorsal interosseous)	4+ (thumb abduction) 5 (first dorsal interosseous)
Muscle weakness LE	1 (foot dorsiflexion) 2 (foot plantar flexion)	2 (foot dorsiflexion, left) 4+ (foot dorsiflexion, right) 5 (foot plantar flexion)
Deep tendon reflexes	Absent	Absent
Pinprick sensation	Decreased at left toe	Decreased up to left ankle
Vibration sense	Decreased up to knees	Decreased at left toe
Position sense	Reduced at right toe	Decreased at toes
Romberg's test	Present	Present
Gait pattern	Steppage	Steppage
Pes cavus	High arches	None
Ulnar nerve MNCV	50 m/s	45 m/s
Ulnar nerve CMAP	4.1 mV	6.7 mV
Radial SNAP	Absent	3.1
CMTNSv2	16/36	10/36
Other features	Prostate cancer	Colon cancer, prostate cancer

CMAP, compound muscle action potential; CMTNSv2, Charcot-Marie-Tooth neuropathy score version 2; Distal, muscle groups below elbow/knee; LE, lower extremity; M, male; NCS, nerve conduction studies; MNCV, motor nerve conduction velocity; Proximal, muscle groups above elbow/knee; SNAP, sensory nerve action potential; UE, upper extremity.

with an adenovirus vector. In our previous study, *Kif1a*^{+/-} mice developed progressive sensory nerve palsy at age 7–12 months and impaired pain sensation at age 5 months (Tanaka *et al*, 2016). It has also been confirmed that the protein content of KIF1A in 10-month-old *Kif1a*^{+/-} mouse DRG is reduced to approximately 1/4, and the distribution of surface TrkA is also reduced (Tanaka *et al*, 2016). Immunofluorescence experiments consistently showed that the cell-surface TrkA signal density was significantly lower in *Kif1a*^{+/-} DRG neurons than in *Kif1a*^{+/+} DRG neurons (Fig 2A). This phenotype in *Kif1a*^{+/-} neurons was rescued by overexpression of KIF1A-EGFP but was less effectively rescued by KIF1A (E239K)-EGFP (Fig 2A).

Similarly, the expression of TRPV1, a capsaicin receptor presented on the cell surface by the NGF-TrkA signaling system,

was also significantly reduced in *Kif1a*^{+/-} DRG neurons compared with *Kif1a*^{+/+}, and this phenotype could be rescued by KIF1A-EGFP but not by KIF1A(E239K)-EGFP (Fig 2B). Furthermore, the expression of the synaptic vesicle proteins Rab3A, synaptotagmin, and DENN/MADD was significantly decreased in *Kif1a*^{+/-} neurons compared with *Kif1a*^{+/+} neurons, and KIF1A (E239K)-EGFP did not increase the localization of these proteins, unlike KIF1A-EGFP (Fig 2C–E). No such tendency was observed for the control tubulin (Fig 2F). To confirm that the observed neurites were axons but not dendrites, we cultured DRG neurons from *Kif1a*^{+/+} and *Kif1a*^{+/-} mice on microfluidic chambers (Appendix Fig S1). The assessments of KIF1A motors levels are shown in Fig EV1.

Next, we performed live imaging of ECFP-TrkA, TagRFP-Rab3QL, and TagRFP-synaptotagmin in *Kif1a*^{+/-} DRG neurons when KIF1A or KIF1A(E239K) were overexpressed. As a result of focusing on anterograde transport, the velocity of TrkA was $1.29 \pm 0.49 \mu\text{m/s}$ (mean \pm SD) for *Kif1a*^{+/+} mouse DRG neurons and $0.74 \pm 0.38 \mu\text{m/s}$ for *Kif1a*^{+/-} neurons (red graphs in Fig 2G), which was consistent with our previous report (Tanaka *et al*, 2016). Overexpression of KIF1A recovered the velocity to $1.13 \pm 0.43 \mu\text{m/s}$, but KIF1A (E239K) overexpression resulted in a velocity of $0.60 \pm 0.28 \mu\text{m/s}$, which did not rescue the slow velocity phenotype (Figs 2G and EV2A). The same tendency was observed with Rab3QL, a Rab3 mutant that mimics the active and transportable GTP form (Niwa *et al*, 2008), and synaptotagmin (Figs 2H and I, and EV2B and C), while the motility of mitochondria which are known cargoes that depend on KIF5 (Tanaka *et al*, 1998) was constant under all conditions (Figs 2J and EV2D). Changes in motility due to overexpression of KIF1A or KIF1A(E239K) were not found in the less frequently observed retrograde movements of TrkA, Rab3QL, synaptotagmin, and mitochondria (Blue graphs in Fig 2G–J). These results consistently demonstrate that the $\beta 7$ mutation interferes with phenotype rescue in *Kif1a*^{+/-} axons, suggesting that it impairs proper localization of these cargoes.

The $\beta 7$ mutation E239K slows down the anterograde motility of KIF1A in neurons

Next, to investigate the difference in axonal transport between the WT and the mutant, we conducted live imaging of KIF1A-EGFP and $\beta 7$ mutant KIF1A(E239K)-EGFP using primary cultures of DRG neurons. Twenty-four to 30 h after transduction with the adenoviral vector, axonal transport approximately 150 μm away from the cell body was visualized using a confocal laser scanning microscope (Fig 3A). Movements of signal particles were observed in both samples (Fig 3B). However, the velocity of the anterograde movement of KIF1A(E239K)-EGFP was 25% slower than that of KIF1A-EGFP, as quantified with a kymograph [KIF1A-EGFP: $2.4 \pm 0.42 \mu\text{m/s}$ (mean \pm SD); KIF1A(E239K)-EGFP: $1.8 \pm 0.30 \mu\text{m/s}$] (Fig 3C and D, and Movie EV1). The direction of KIF1A-EGFP and KIF1A (E239K)-EGFP signal movements was similar; almost 90% moved anterogradely, and approximately 10% moved retrogradely (Fig 3E). Collectively, these results indicate that in DRG neurons, the $\beta 7$ mutation in KIF1A induces deterioration in the speed of anterograde transport without affecting directionality.

We then cotransduced the KIF1A knockdown vector and RNAi immune KIF1A-EGFP or KIF1A(E239K)-EGFP expression vectors

Table 2. Characterization of the mutation and the details of the exome sequencing.

Confirmed mutation	Mutated gene	Position	Amino acid change	Zygosity	Inheritance	Allele frequency
	KIF1A	chr2:240784994 (GRCh38.p12)	E239K	Heterozygote	Autosomal dominant	0.00003941
Analysed genes	AARS (NM_001605.2)	DNAJB2 (NM_001039550.1)	GLA (NM_000169.2)	MCM3AP (NM_003906.4)	POLG2 (NM_007215.3)	SLC52A3 (NM_033409.3)
	AIFM1 (NM_004208.3)	DNM2 (NM_001005360.2)	GNB4 (NM_021629.3)	MED25 (NM_030973.3)	PRDM12 (NM_021619.2)	SLC5A7 (NM_021815.2)
	APOA1 (NM_000039.2)	DNMT1 (NM_001130823.1)	GSN (NM_000177.4)	MFN2 (NM_014874.3)	PRPS1 (NM_002764.3)	SMN1 (NM_000344.3)
	ASAH1 (NM_177924.3)	DRP2 (NM_001939.2)	HARS (NM_002109.5)	MME (NM_007289.2)	PRX (NM_181882.2)	SMN2 (NM_017411.3)
	ATL1 (NM_015915.4)	DST (NM_001723.5; NM_015548.4)	HEXA (NM_000520.4)	MORC2 (NM_001303256.2)	RAB7A (NM_004637.5)	SPG11 (NM_025137.3)
	ATL3 (NM_015459.4)	DYNC1H1 (NM_001376.4)	HINT1 (NM_005340.6)	MPZ (NM_000530.6)	REEP1 (NM_022912.2)	SPTLC1 (NM_006415.3)
	ATP1A1 (NM_000701.7)	EGR2 (NM_000399.3)	HMBS (NM_000190.3)	MTMR2 (NM_016156.5)	RETREG1 (NM_001034850.2)	SPTLC2 (NM_004863.3)
	ATP7A (NM_000052.6)	ELP1 (NM_003640.3)	HSPB1 (NM_001540.3)	NDRG1 (NM_006096.3)	SBF1 (NM_002972.3)	SURF1 (NM_003172.3)
	BAG3 (NM_004281.3)	EXOSC9 (NM_001034194.1)	HSPB8 (NM_014365.2)	NEFH (NM_021076.3)	SBF2 (NM_030962.3)	TFG (NM_006070.5)
	BICD2 (NM_001003800.1)	FBLN5 (NM_006329.3)	IGHMBP2 (NM_002180.2)	NEFL (NM_006158.4)	SCN11A (NM_014139.2)	TRIM2 (NM_001130067.1)
	BSC12 (NM_032667.6)	FBXO38 (NM_030793.4)	INF2 (NM_022489.3)	NGF (NM_002506.2)	SCN9A (NM_002977.3)	TRPV4 (NM_021625.4)
	CHCHD10 (NM_213720.2)	FGD4 (NM_139241.3)	KIFIA (NM_004321.6)	NTRK1 (NM_001012331.1)	SEPT9 (NM_006640.4)	TTR (NM_000371.3)
	COX6A1 (NM_004373.3)	FIG4 (NM_014845.5)	KIF5A (NM_004984.2)	PDK3 (NM_001142386.2)	SH3TC2 (NM_024577.3)	UBA1 (NM_003334.3)
	CYP27A1 (NM_000784.3)	GAN (NM_022041.3)	LITAF (NM_004862.3)	PLEKHG5 (NM_020631.4)	SIGMAR1 (NM_005866.3)	VAPB (NM_004738.4)
	CYP7B1 (NM_004820.3)	GARS (NM_002047.2)	LMNA (NM_170707.3)	PMP2 (NM_002677.3)	SLC12A6 (NM_133647.1)	VRK1 (NM_003384.2)
	DCTN1 (NM_004082.4)	GDAP1 (NM_018972.2)	LRSAM1 (NM_138361.5)	PMP22 (NM_000304.3)	SLC25A46 (NM_138773.2)	WNK1 (NM_213655.4)
	DHTKD1 (NM_018706.6)	GJB1 (NM_000166.5)	MARS (NM_004990.3)	POLG (NM_002693.2)	SLC52A2 (NM_024531.4)	YARS (NM_003680.3)

into *Kif1a*^{+/+} DRG neurons to measure the anterograde transport velocity in an environment that eliminates the effects of endogenous KIF1A (Fig 3F). The knockdown vector, which was used in a previous study (Tanaka *et al.*, 2016), was confirmed by immunocytochemistry to reduce KIF1A levels in DRG cells (Appendix Fig S2). The movement of KIF1A(E239K)-EGFP in KIF1A knockdown DRG axons was significantly slower than that of KIF1A-EGFP (Fig 3F and G). Interestingly, the velocity of KIF1A(E239K)-EGFP was not significantly different from that of the scrambled control (Fig 3G). This suggests that the phenotype does not deteriorate even when KIF1A (E239K)-EGFP is the only source of the KIF1A motor.

The $\beta 7$ mutation E239K induces deficits in the motor activity of KIF1A *in vitro*

To investigate the effect of the E239K mutation on KIF1A motor activity, we first performed a microtubule gliding assay on

KIF1A382 proteins (aa 1-382 with His-tag) coated on glass *in vitro*. KIF1A382 (WT and E239K) constructs composed of the motor domain, the neck-linker, and the neck-coil were bacterially expressed and purified. The gliding of rhodamine-labeled and taxol-stabilized microtubules was monitored by TIRF microscopy. The microtubule gliding velocity caused by E239K was slower than that caused by WT (Fig 4A and Movie EV2), and 13% of the microtubules on E239K stopped for more than 3 s (Fig 4B). From the slope of the kymographs, the gliding velocities caused by WT and E239K were calculated as $1.20 \pm 0.24 \mu\text{m/s}$ (mean \pm SD) and $0.943 \pm 0.28 \mu\text{m/s}$, respectively, so the gliding velocity caused by E239K was 22% slower than that caused by the WT (Fig 4C and H). These reconstituted *in vitro* assays clearly suggest that the E239K mutation causes fundamental deficits in motor activity through internal mechanochemical failure within the KIF1A protein.

How does the E239K mutation cause deficits in motor activity? Microtubule gliding velocity by kinesin motors is closely linked with

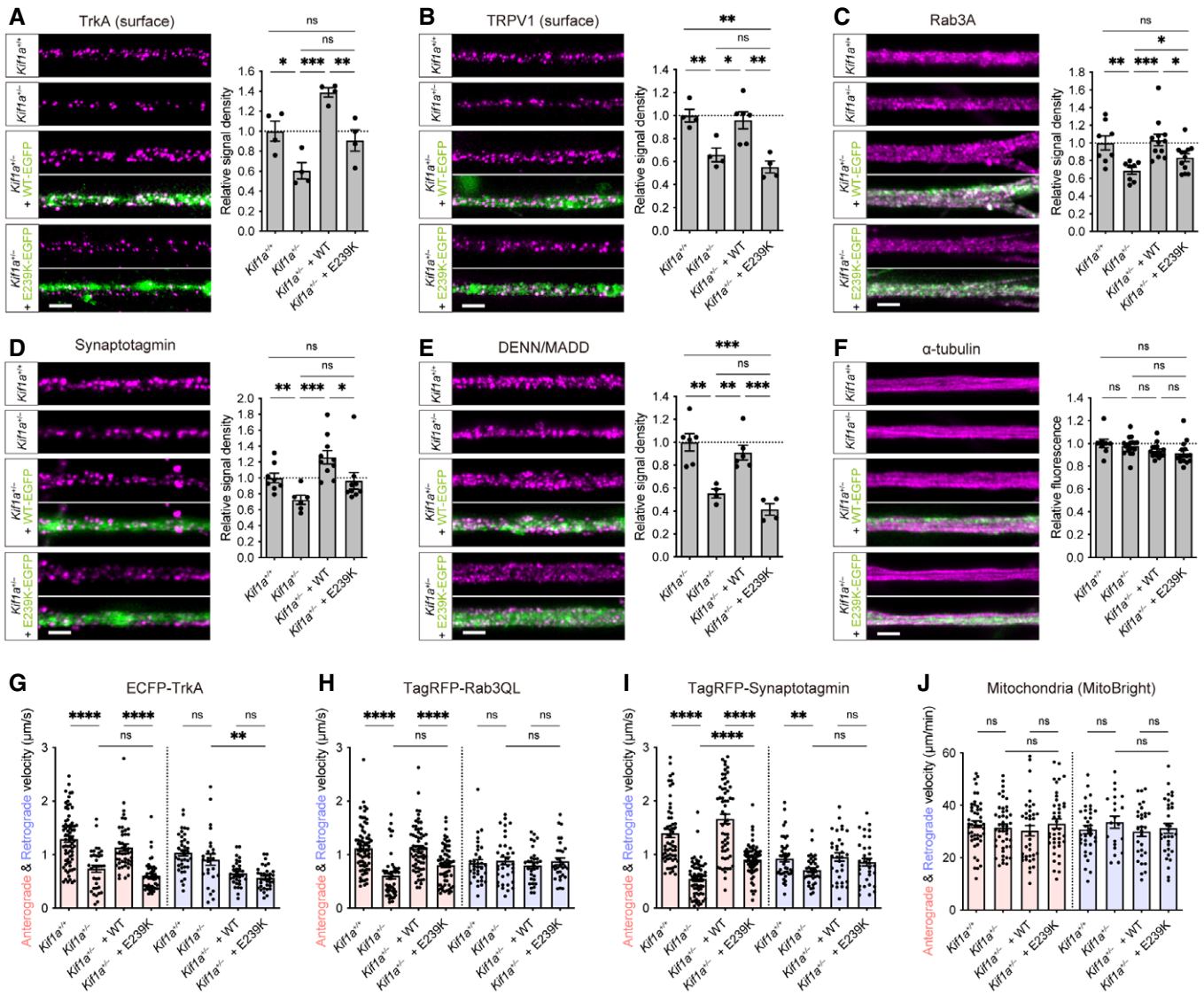


Figure 2. Axonal transport of KIF1A cargoes by the WT and the β 7 mutant E239K.

A–F Immunocytochemistry of DRG neurons and the corresponding quantifications of the indicated genotypes for surface TrkA (A), surface TRPV1 (B), Rab3A (C), synaptotagmin (D), DENN/MADD (E) and α -tubulin (F). TrkA and TRPV1 were visualized without permeabilization. ns, $P > 0.05$; * $P < 0.05$; ** $P < 0.01$; *** $P < 0.001$; Welch's t test from at least three independent cultures. Error bars show SEM. Scale bars, 2 μ m.

G–J Anterograde (red) and Retrograde (blue) velocities of ECFP-*TrkA* (G), TagRFP-*Rab3QL* (H), TagRFP-*synaptotagmin* (I), and mitochondria labeled with MitoBright (J). ns, $P > 0.05$; ** $P < 0.01$; **** $P < 0.0001$. ECFP-*TrkA*, $n = 25$ –72; TagRFP-*Rab3QL*, $n = 31$ –71; TagRFP-*synaptotagmin*, $n = 33$ –62; Mitochondria, $n = 21$ –49 moving particles were quantified from at least three independent cultures and statistical analysis performed using unpaired t test. Error bars show SEM.

Source data are available online for this figure.

microtubule-activated ATPase activity and the binding affinity with microtubules (Howard *et al*, 1989). To verify whether the decreased velocity of this mutant is due to its defect in ATP hydrolysis activity or in binding affinity with microtubules, we compared the microtubule-stimulated ATPase activity of WT and E239K KIF1A382. E239K showed 27% lower ATPase activity than the WT [k_{cat} (WT) = $139 \pm 4.8/s$ (mean \pm SE); k_{cat} (E239K) = $101 \pm 2.8/s$] (Fig 4D and H). This decreased ratio of ATPase rates is almost the same as that of the ratio of the microtubule gliding velocities. On the other hand, the apparent Michaelis–Menten constant (K_m) of

E239K was close to that of WT [K_m (E239K) = 12.1 ± 2.4 nM; K_m (WT) = 11.9 ± 3.0 nM (mean \pm SE)], indicating that the E239K mutant and WT motors have similar affinities for microtubules. These *in vitro* data collectively indicate that the E239K mutation does not induce changes in microtubule-binding affinity but limits the enzymatic cycle of ATP hydrolysis turnover, which can decrease the velocity.

Next, to elucidate the effect of the E239K mutation more precisely on the ATP hydrolysis cycle, nucleotide-free states KIF1A382 (WT and E239K) were rapidly mixed with mant-ATP in the stopped-flow fluorometer, and the association and dissociation of mant-ATP

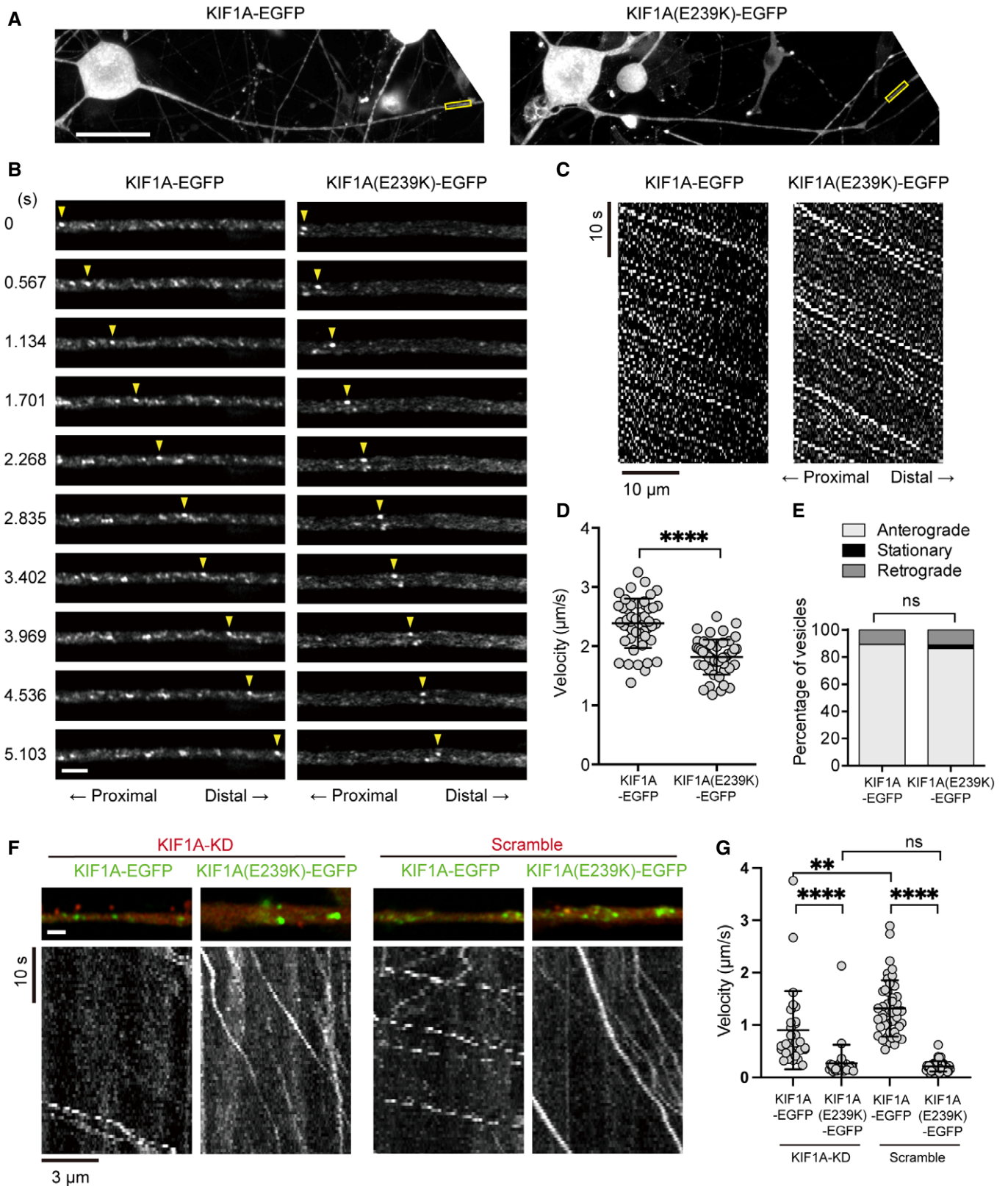


Figure 3.

Figure 3. Live-cell imaging of the WT KIF1A and the $\beta 7$ mutant E239K.

- A Fluorescence images of dissociated mouse DRG neurons at DIV5 transduced with adenoviral vectors encoding KIF1A-EGFP and KIF1A(E239K)-EGFP. The boxes show the axonal area for the time-lapse images. Scale bar, 50 μm .
- B, C Time-lapse fluorescence images of DRG neurons expressing KIF1A-EGFP and KIF1A(E239K)-EGFP (B) and representative kymographs of signal movements (C). Arrowheads in (B) show the anterogradely moving particles. Scale bar in (B), 2 μm . See Movies EV1 and 2.
- D Velocities of the moving particles calculated from the slopes of the kymographs. Data are shown as mean and SD from $n = 49$ moving particles of three independent cultures. **** $P < 0.0001$; Unpaired t test.
- E Direction of the moving particles at the start of observation. ns, $P = 0.1484$; chi-square test.
- F Movements of KIF1A-EGFP and KIF1A(E239K)-EGFP expressed in KIF1A knockdown DRG and the scrambled control. White scale bar, 1 μm .
- G Anterograde velocities of the indicated genotypes calculated from the kymograph slopes. Data are shown as mean and SD. KD+KIF1A-EGFP, $n = 29$; KD+KIF1A(E239K)-EGFP, $n = 32$; scrambled+KIF1A-EGFP, $n = 44$; scrambled+KIF1A(E239K)-EGFP, $n = 42$ from three independent cultures. ns, $P = 0.3329$; ** $P < 0.01$; **** $P < 0.0001$; Unpaired t test.

Source data are available online for this figure.

with KIF1A (WT and E239K) were monitored (Fig 4E). As a result, the association rate was higher in E239K, while the dissociation rate was lower than that of WT (Fig 4F and H). In addition, the dissociation of mant-ADP from KIF1A (WT and E239K) were also measured in an excess of unlabeled ATP with or without microtubule. Interestingly, the dissociation from E239K was slower than that from WT (Fig 4G and H). Taken these data together, E239K caused the enhanced association of ATP with KIF1A, and delayed the release of ADP from the KIF1A motor during ATP hydrolysis.

In previous studies, KIF1A was reported to form dimer states from an inactivated monomer state to undergo processive stepping toward microtubule plus-end by microtubule-activated ATP hydrolysis. A recent kinesin-3 KIF13B paper has shown that the CC1 region at the C-terminal of the neck-coil is essential for autoinhibited structure (Ren *et al*, 2018a). Therefore, we investigated the effect of the E239K mutation on autoinhibition and dimerization activity of KIF1A. KIF1A382 (MD-NL-NC), KIF1A400 (MD-NL-NC-Hinge, residue 1–400), and KIF1A472 (MD-NL-NC-Hinge-CC1, residue 1–472) were bacterially expressed, purified, and assayed by analytical size exclusion chromatography (Fig EV3). KIF1A382 was present in the monomeric state, while KIF1A400 was predominantly present in a dimeric state for both WT and E239K. In contrast, some population of KIF1A472 exhibited the monomeric form both in WT and in E239K, confirming that the extended CC1 domain has a suppressing effect on dimerization activity as expected from the previous report

on KIF13B (Ren *et al*, 2018a). These results suggested that the E239K mutation does not significantly affect dimerization and auto-inhibition activity by the CC1 region.

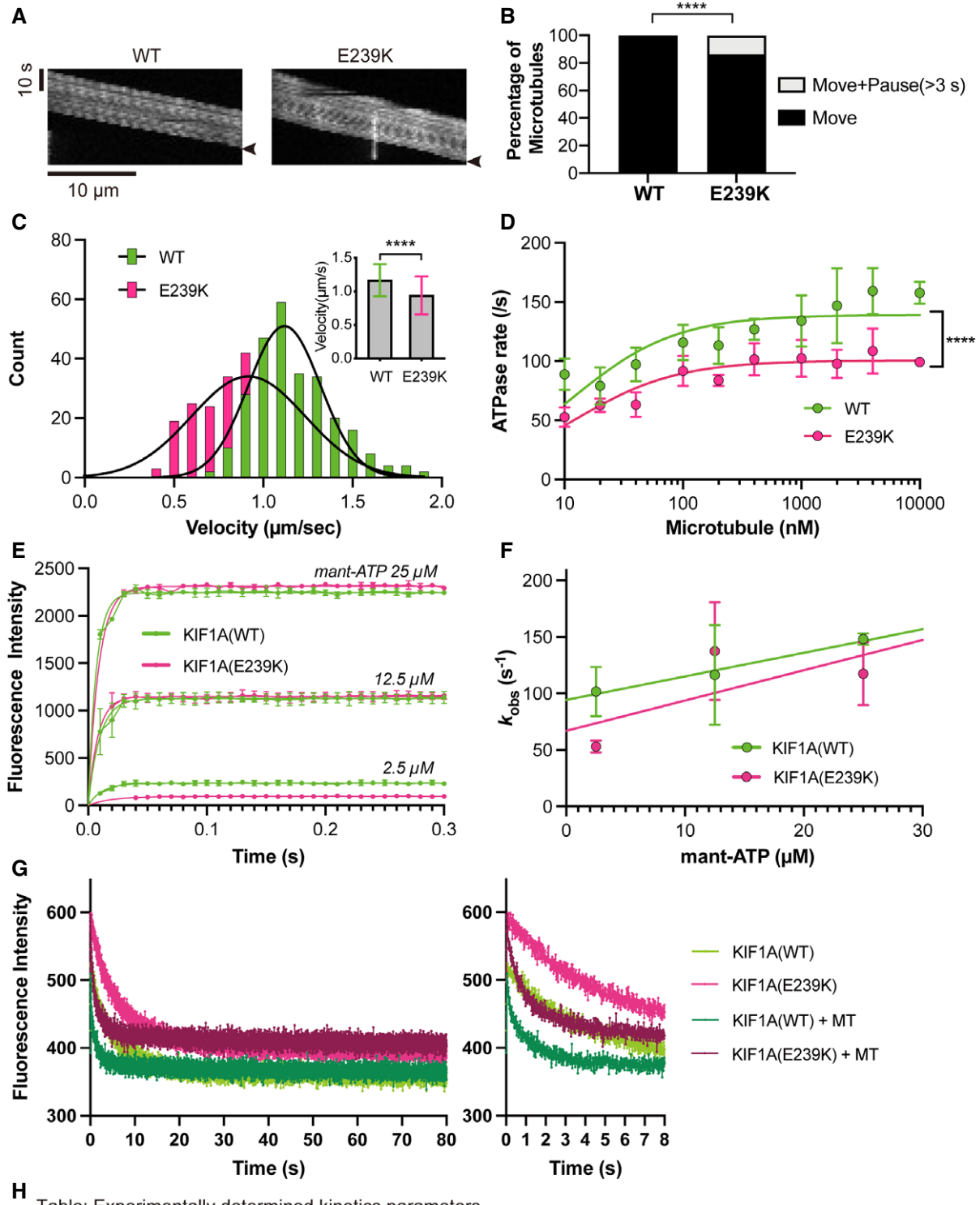
The $\beta 7$ mutation E239K disturbs the proper coordination of the motor domain and the neck domain

Then how does the E239K mutation induce a delay in the ATP hydrolysis cycle? To examine the intramolecular structural relationship around E239/K239, we first conducted X-ray crystallography of KIF1A382 (WT and E239K), which contains the entire neck domain. Crystals were obtained docked with the nucleotide analogue ADP-aluminum fluoride (ADP-AlFx), which mimics the late transitional state of ATP hydrolysis (Fig 5A). Resolutions of 2.57 and 1.76 \AA were achieved for the WT and the E239K mutant, respectively (Table 3). In both structures, E239/K239 was located on $\beta 7$, oriented close to the boundary between the neck-linker and the neck-coil, and it was located outside the nucleotide- and microtubule-binding domains (Fig 5A and Appendix Fig S3A). The neck-linker was fully docked to the catalytic core, and the subsequent neck-coil was formed along $\beta 7$ and L10. These docked conformations of WT and E239K in the hydrolysis transition state were basically consistent with previously reported structures with a docked neck-linker: chimeric KIF1A-C340 (KIF1A motor domain plus KIF5C neck-linker, PDB: 1VFX) (Nitta *et al*, 2004) (Appendix Fig S3B–D), KIF1A complexed with a microtubule (PDB: 4UXR)

Figure 4. Effect of the $\beta 7$ mutant E239K on KIF1A motility and kinetics *in vitro*.

- A Representative kymographs of tetramethylrhodamine-labeled microtubule movement driven by the WT and the E239K mutant. The arrowheads represent the end positions of the WT and E239K.
- B Movement of microtubules on glass driven by the WT and E239K. **** $P < 0.0001$, chi-square test.
- C Microtubule gliding velocity of the WT (green) and E239K mutant (magenta) determined by kymograph slope. Data and error bars in the inserted graph are presented as the mean \pm SD. $n = 269$ microtubules for WT, $n = 263$ microtubules for E239K. **** $P < 0.0001$, unpaired t test.
- D ATPase activity of WT (green) and E239K mutant (magenta) activated by microtubules. Data are represented as the mean \pm SD. The data from at least three independent experiments were analyzed. **** $P < 0.0001$, two-way ANOVA.
- E Measurements of the association and dissociation of mant-ATP. Nucleotide-free KIF1A(WT) and KIF1A(E239K) (final concentrations 2 μM) were rapidly mixed with varying concentrations of mant-ATP (2.5–25 μM) in a stopped-flow fluorometer. Representative transients at 25 μM , 12.5 μM , and 2.5 μM mant-ATP and fitted single-exponential function curves are shown. Data are represented as the mean \pm SD. The data from three independent measurements were analyzed.
- F Rate constants (k_{obs}) determined for the reaction of mant-ATP with nucleotide-free KIF1A(WT) and KIF1A(E239K) were plotted against concentration of mant-ATP. Data are represented as the mean \pm SD. The data from three independent measurements were analyzed.
- G Measurements of the dissociation of mant-ADP for 80 s (left panel) and the enlarged view for the first 8 s (right panel). KIF1A(WT) and KIF1A(E239K) (final concentrations 50 μM) preloaded with mant-ADP were mixed into an excess of unlabeled ATP (5 mM) with or without taxol-microtubule. Fluorescence decreases were observed upon the dissociation of mant-ADP.
- H Summary of the experimentally determined kinetics parameters of KIF1A(WT) and KIF1A(E239K). Data are represented as the mean value \pm SD for mant-ATP measurements.

Source data are available online for this figure.



construct	Microtubule	Kinesin ATPase assay		mant-ATP association & dissociation		mant-ADP dissociation	
	gliding assay	MT (+)		MT (-)		MT (-)	MT (+)
		velocity ($\mu\text{m}\cdot\text{s}^{-1}$)	k_{cat} (s^{-1})	K_m (nM)	k_{+1} ($\mu\text{M}^{-1}\text{s}^{-1}$)	k_{-1} (s^{-1})	k_{obs} (s^{-1})
KIF1A(WT)	1.20 ± 0.241	139 ± 4.85	11.9 ± 3.01	2.08 ± 0.965	94.3 ± 15.6	0.167	0.538
KIF1A(E239K)	0.943 ± 0.282	101 ± 2.84	12.1 ± 2.44	2.68 ± 1.47	66.9 ± 23.8	0.141	0.504

Figure 4.

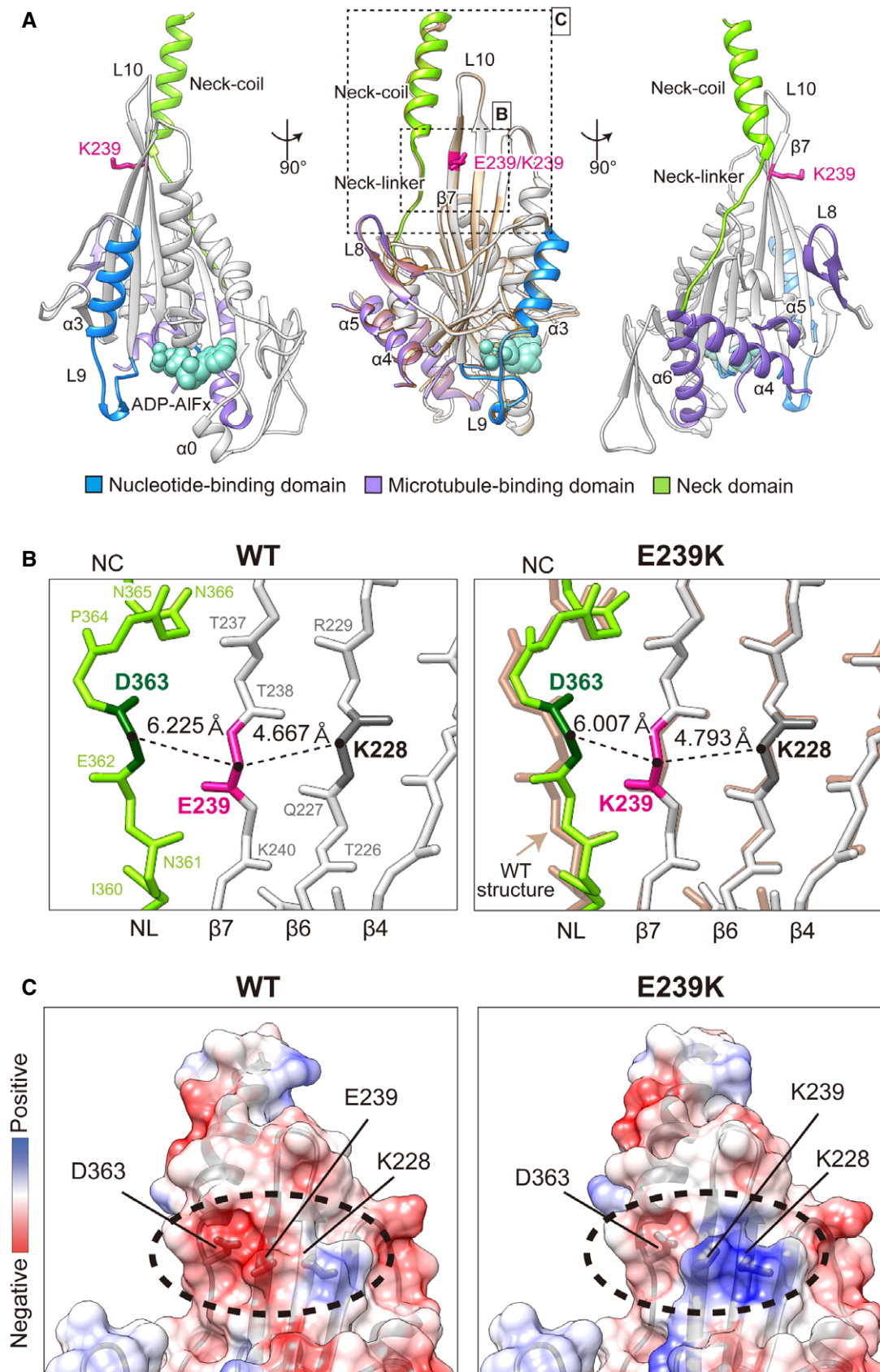


Figure 5.

Figure 5. The adjacent positions of the E239K mutation on $\beta 7$ and the neck domain.

- A Overall E239K structure. The WT structure is superimposed in the central panel in brown. The location of E239/K239 is shown in magenta, the nucleotide-binding domain (residues 98–102 and 189–216) is shown in blue, the microtubule-binding domain (residues 168–178, 249–309 and 335–353) is shown in purple, and the neck domain (residues 354–381) is shown in green.
- B Comparison of the WT (left) and E239K (right) around E239/K239. E239 and K239 are located on $\beta 7$ and sandwiched between D363 of the neck-linker and $\beta 6$ K228. The $C\alpha$ - $C\alpha$ distances of D363-E239/K239 and E239/K239-K228 were measured and are shown. NC, neck-coil; NL, neck-linker. The WT model is superimposed on the E239K model in brown.
- C Electrostatic charge distributions shown by the surface model. The regions of charge changes are indicated by dotted circles. Negative and positive charges are shown in red and blue, respectively.

Table 3. Data collection of X-ray crystallography and refinement statistics.

	WT	E239K mutant
Data collection statistics		
X-ray source	SPring8-BL41XU	SPring8-BL41XU
Space group	P2 ₁ 2 ₁ 2 ₁	P2 ₁ 2 ₁ 2 ₁
Unit cell parameters		
a, b, c (Å)	41.502, 57.319, 154.826	41.655, 57.249, 155.041
α , β , γ (°)	90.000, 90.000, 90.000	90.00, 90.00, 90.00
Wavelength (Å)	1	1
Resolution limits (Å) ^A	30.00-2.57 (2.63-2.57)	30.00-1.76 (1.82-1.76)
No. of unique reflections	11987 (859)	36686 (3095)
Completeness (%)	96.8 (100.0)	97.7 (84.7)
Redundancy	6.1 (6.5)	5.9 (5.2)
R _{merge} (%) ^B	8.1 (51.7)	5.4 (64.2)
R _{p.i.m} (%)	6.3 (30.7)	4.0 (37.6)
Mean I/ σ (I)	10.1 (1.8)	13.4 (0.9)
Refinement statistics		
Resolution limits (Å)	30.00-2.57	30.00-1.76
R _{work} (%) ^C /R _{free} (%) ^D	22.8/23.7	21.5/24.0
Rmsd for bonds (Å)	0.0072	0.0094
Rmsd for angles (°)	1.5293	1.6395
Wilson B-factor (Å ²)	39.9	22.6
No. of non-hydrogen protein atoms	2777	2768
No. of water oxygen atoms	24	107
Ramachandran plot (%)		
Most favored regions	90.72	94.46
Additional allowed regions	9.28	5.24
PDB entry	7EO9	7EOB

^AValues in parentheses are for the highest resolution shell. About 5% of total reflections are used for highest resolution shell calculations.

^BR_{merge} = $\sum h \sum l |I_h - \langle I_h \rangle| / \sum h \sum l \langle I_h \rangle$, where I_h is the l th observation of reflection h and $\langle I_h \rangle$ is the weighted average intensity for all observations l of reflection h .

^CR_{work} factor = $\sum h \sum l |F_{obs}(h) - F_{cal}(h)| / \sum h \sum l |F_{obs}(h)|$, where $F_{obs}(h)$ and $F_{cal}(h)$ are the observed and calculated structure factors for reflection h respectively.

^DR_{free} factor was calculated same as R_{work} factor using the 5% the reflections selected randomly and omitted from refinement.

(Atherton *et al*, 2014) (Appendix Fig S4A), KIF5B (PDB: 1MKJ) (Sindelar *et al*, 2002) (Appendix Fig S4B) and KIF5C (PDB: 2KIN) (Sack *et al*, 1997) (Appendix Fig S4C).

Compared to the structures of KIF13B (PDB codes: 5ZBR, 6A1Z, 6A20) (Ren *et al*, 2018a, 2018b), which is also a member of the kinesin-3 family, the neck-coil of our structure adopted a new structure (Fig EV4). The neck-coil in our ADP-AlFx state structure pointed to an intermediate angle between that in the AMPPNP state and that in the ADP state (Fig EV4A). This structure may be due to differences in nucleotide states or crystal packing, but in any case, the $\beta 7$ E239 seemed to interact with the neck domain at close range (Fig EV4B and C). E239 was also close to the root of the folded conformation of the neck-coil and CC1a in the inhibited structure of KIF13B (PDB ID 6A20) (Ren *et al*, 2018a; Fig EV4C and D).

The $C\alpha$ - $C\alpha$ distance between $\beta 7$ (E239 in WT, K239 in mutation) and the neck-linker (D363) became shorter in the mutant (WT, 6.225 Å; E239K mutant, 6.007 Å; Fig 5B). The electrostatic surface potential showed that the E239K mutation contributed to a patch of electropositive charge on the originally negatively charged region on the motor domain that could maintain the appropriate electrostatic balance with the negatively charged neck domain (Fig 5C).

Consistently, the B-factor of the neck domain, which indicates the degree of atomic flexibility in the three-dimensional dynamic structure, was significantly different between the WT and E239K (Appendix Fig S5A and B). The B-factor difference between the WT and mutant in the neck-linker and the neck-coil was greater than that in other regions (Appendix Fig S5C). This indicated that the relative intramolecular flexibility in the neck domain was smaller in the mutant than in the WT, supporting our model that the $\beta 7$ mutation E239K has a stronger affinity between the motor and neck domains.

In addition, slight structural changes between WT and E239K mutant were observed in two clusters on both sides of the central β -sheet: residues near the mutation (box (i); $\beta 7$, L10, neck-linker, and neck-coil) and the nucleotide-binding pocket (box (ii); $\alpha 3$ -L9 and L5) (Fig EV5). This indicated that the $\beta 7$ mutation affects the appropriate coordination and electrostatic dynamics of the neck, which are produced by structural transmission from ATP hydrolysis at the nucleotide-binding pocket across the motor domain to the neck domain.

The $\beta 7$ mutation E239K produces an excessive affinity between the neck domain and $\beta 7$ of the catalytic core

We next quantified the site-specific and dynamic interaction between the neck and the motor domain in solution using the WT and the E239 mutant to elucidate the rate-limiting step in three typical hydrolysis states (nucleotide-free state, the early transitional state with ADP-BeFx, and the late transition state with ADP-AlFx)

during the ATP hydrolysis cycle (Fisher *et al*, 1995; Ogawa *et al*, 2017). The site-specific interaction was quantitatively analyzed by the combination of a protein-painting technique (Luchini *et al*, 2014; Haymond *et al*, 2019) and the site-specific quantitation of kinesin proteins (Ogawa & Hirokawa, 2015) based on mass spectrometry. When KIF1A382 (WT or E239K) complexed with polymerized microtubules in each nucleotide state was coated with the painting dye FBB, the domain–domain interfaces tightly covered by the specific interaction remained unpainted. After tryptic digestion, peptides from unpainted interfaces were identified by an LC-MS/MS system. For relative quantitation of interaction sites, each peptide solution was labeled with differential stable isotope tags (Tandem Mass Tag, TMT-tags). The MS/MS fragments were simultaneously used to identify the fragments and to quantify the relative level of each peptide by the intensities of the unique reporter ions from the TMT-tags. As a result, fragments containing $\beta 7$ ($\beta 6$ -L10- $\beta 7$) and the neck-coil were identified as unpainted regions, and the relative quantitation values showed dynamic trends in $\beta 7$ -neck docking (Fig 6A). The association between $\beta 6$ -L10- $\beta 7$ and the neck-coil of WT increased until it peaked in the strong docking state mimicked by ADP-BeFx [1.61-fold ($\beta 6$ -L10- $\beta 7$) and 2.55-fold (neck-coil) compared to that in the nucleotide-free state] and showed a significant decline in the ADP-AIFx state [0.93-fold ($\beta 6$ -L10- $\beta 7$) and 0.61-fold (neck-coil) compared to that in the nucleotide-free state] (graphs in grey, Fig 6B and D). On the other hand, the association between $\beta 6$ -L10- $\beta 7$ and the neck-coil of the $\beta 7$ mutant E239K gradually increased or remained flat even in the late transitional state with ADP-AIFx [$\beta 6$ -L10- $\beta 7$, 2.48-fold in the ADP-BeFx state and 4.33-fold in the ADP-AIFx state; neck-coil, 1.76-fold in the ADP-BeFx state and 1.82-fold in the ADP-AIFx state] (graphs in black, Fig 6C and D). These data suggest that the $\beta 7$ mutant E239K may interfere with the rapid dissociation of the neck domain from $\beta 6$ -L10- $\beta 7$ of the motor domain, thereby delaying ATP hydrolysis turnover. A similar tendency was also observed in the peripheral regions of the neck-linker ($\alpha 1$ - $\beta 3$ -P loop, $\alpha 4$ -L12 (K loop), and L12- $\alpha 5$) (Fig 6A and Appendix Fig S6). Together with the low ATP hydrolysis rate of the mutant (Fig 4H), these data suggest that excessive interaction between the neck domain and motor domain components, such as $\beta 7$, might delay the catalytic ATP hydrolysis cycle.

Taking these pieces of evidence from diseases to atomic structures together with previous studies, we conclude here that the $\beta 7$ mutation E239K might interfere with the electrostatic balance between the motor and neck domains, producing excessive affinity in a docked conformation (Fig 6E). This molecular mechanical failure will cause a delay in the ATP hydrolysis cycle, finally resulting in slowed intracellular transport in neurons. $\beta 7$ mutation thus affects motility of KIF1A motor and its transport of cargoes so that

malfunction of KIF1A relates with pathogenesis of a wide variety of human neuropathies including CMT2, SPG30, and HSN2C.

Discussion

KIF1A E239K disease mutation reduces motor activity by influencing ATPase cycle

In this study, we characterized a point mutation E239K in the KIF1A motor, which was identified in a family with hereditary axonal neuropathy CMT2 and was also reported in 24 cases of neuropathies including SPG30 and HSN2C. Our experimental data presented here suggest that this KIF1A mutant is associated with these human neuropathies due to functionally impaired cargo transport in axons. KIF1A motor activity on microtubules was retained but slowed by approximately 20% both *in vivo* and *in vitro* (Figs 3 and 4). Considering the agreement with the differential transport velocities of KIF1A(WT) and KIF1A(E239K) to those of the cargoes, the reductions in localizations of cargoes in the distal axon can likely be explained by the impairment in transport (Figs 2 and EV2). Even slow motors are expected to eventually reach the distal axons. Indeed, overexpression of KIF1A(E239K) in *Kif1a*^{+/-} axons increased the localization of TrkA, Rab3A, and synaptotagmin to the level of *Kif1a*^{+/+} axons (Fig 2A and C, and D). On the other hand, TRPV1 and DENN/MADD had a low rescue effect (Fig 2B and E). These indicate that there may be no increase in transport frequency to compensate for the slow speed, suggesting that cells regulate the entry of KIF1A into axons regardless of the difference in motor speed of approximately 20%. Also, from the quantitative measure of KIF1A motor levels (Fig EV1), the localization of TrkA, TRPV1, Rab3A, synaptotagmin, and DENN/MADD increased in DRG axons with higher expression levels of KIF1A(WT)-EGFP. Similarly, as the expression of KIF1A(E239K)-EGFP increased, the localization of these proteins also increased. The simple linear regression of KIF1A (E239K) was never higher than that of KIF1A(WT) within the measurement range, but our analysis showed that the defects in proteins localization associated with KIF1A(E239K) mutation were improved to some extent with the increase of KIF1A(E239K) level.

The assessment of the KIF1A(E239K) phenotype when KIF1A (E239K) is the sole source of the motor (Fig 3F) indicated that KIF1A(E239K) activity was impaired due to the slow movement of the motor itself, rather than due to making poor dimers or affecting autoinhibition in combination with KIF1A(WT). The effect of KIF1A (E239K) on dimerization and autoinhibited conformation was also

Figure 6. Difference in $\beta 7$ -neck interaction between the WT and the $\beta 7$ mutant E239K.

- A The positions of the $\beta 6$ -L10- $\beta 7$ and neck-coil peptides are shown in brown and green. The positions of the neck-linker peripheral peptides ($\alpha 1$ - $\beta 3$ -P loop, $\alpha 4$ -L12 and L12- $\alpha 5$) are shown in light blue.
- B–D Quantitation of site-specific intramolecular interactions. Representative MS/MS spectra of the indicated peptides, including the mutated amino acid ($\beta 6$ -L10- $\beta 7$) (B and C) and neck-coil (D). In the inserted graphs, the intensities in the ADP-BeFx and ADP-AIFx states were measured with respect to the nucleotide-free state as 1.0. Grey bar graphs, WT; black bar graphs, E239K; (-), nucleotide-free.
- E Schematic diagram of the $\beta 7$ mutation and motor activity. KIF1A moves on microtubules by repeating dynamic structural changes in the neck domain in response to the ATP binding and hydrolysis cycle. The $\beta 7$ mutation exhibits enhanced interaction with the neck-linker and neck-coil and affects motor movement. MT, microtubule; α , α -tubulin; β , β -tubulin; NL, neck-linker; NC, neck-coil.

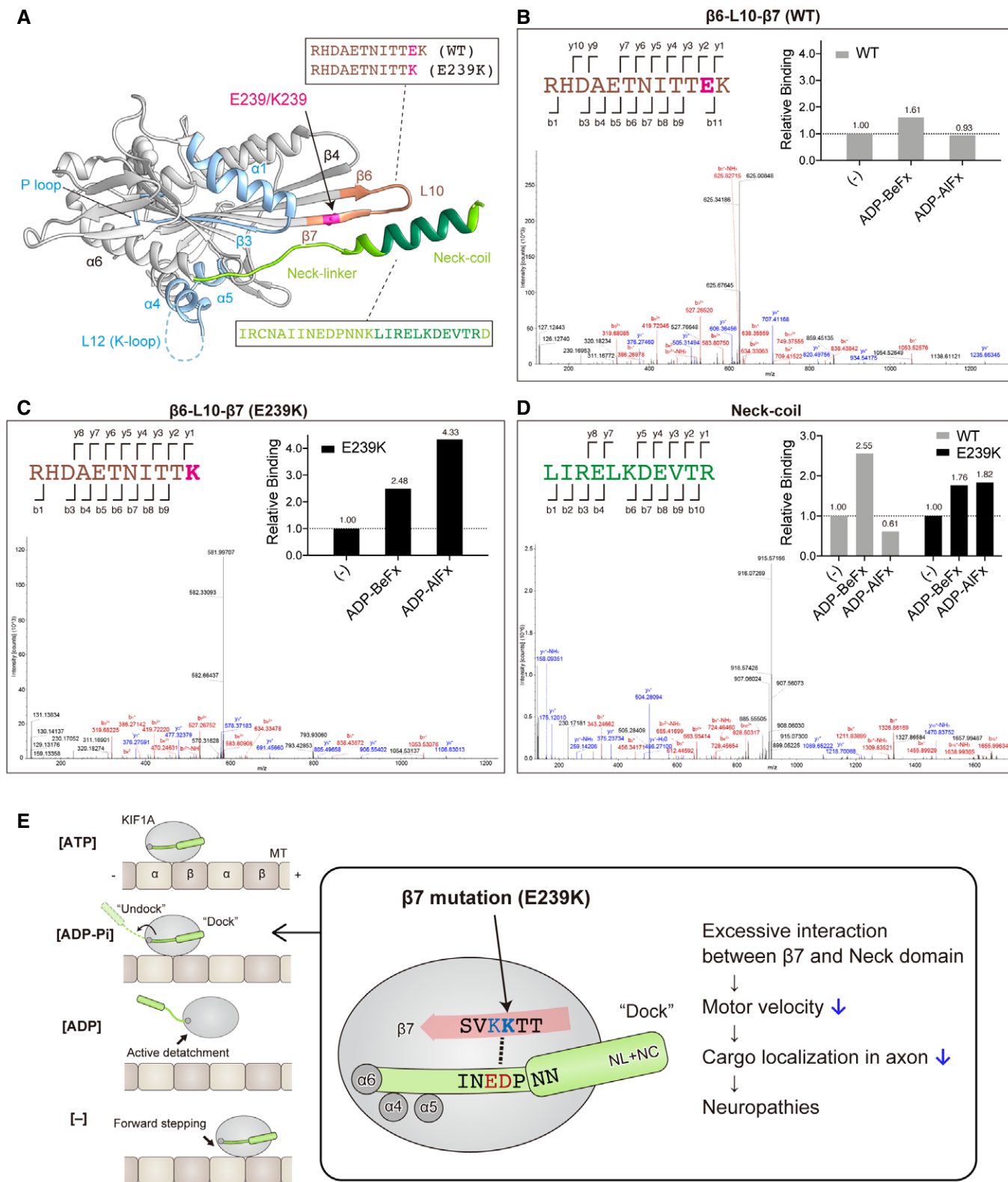


Figure 6.

verified by investigating the oligomeric states of KIF1A constructs including CC1 domain (Fig EV3). The results of increased proportions of KIF1A472 in monomeric state confirmed that NC and CC1

inhibited dimerization (Ren *et al.*, 2018a), but the effects were the same between the WT and E239K mutants. This result was unexpected because E239K is structurally close to the NC and CC1a (Fig

EV4C and D). Further investigation of the physiological dynamic states of full-length KIF1A will answer this question in the future.

Kinetic studies were conducted to clarify the reason for the slow transport of KIF1A(E239K). The ATPase assay revealed that the decrease in transport by E239K was due to a delay in the ATP hydrolysis cycle rather than a change in affinity for microtubules (Fig 4D). However, in a previously reported disease-related mutations of kinesin motors, variants with reduced velocity often have both reduced ATPase activity and reduced microtubule affinity (Jennings *et al*, 2017). Therefore, this E239K mutation provides new insights into the mechanism not only of disease but also of kinesin's catalytic mechanism. Indeed, the precise observation of the KIF1A motor domain and neck domain both at atomic resolution by X-ray crystallography and in dynamic solution by mass spectrometry suggests a model in which the delay in the ATP hydrolysis cycle in this mutant is caused by the excessive electrostatic interaction between $\beta 7$ and the neck domain in the hydrolysis transition state (Figs 5 and 6). Consistently, from the results of the size exclude chromatography experiment, the Stokes radius of KIF1A382, which exists as a monomer, was slightly smaller in E239K (Fig EV3). This data may reflect the affinity of the neck domain and the globular motor domain.

As shown in Fig 6E, KIF1A alternates the orientation of the neck domain (docking/undocking) in a nucleotide-dependent manner while moving on microtubules (Nitta *et al*, 2004; Sindelar & Downing, 2010; Cross, 2016; Hancock, 2016). We demonstrated that the docked neck-linker is close to and oriented toward E239 of $\beta 7$ (Fig 5A) and that in the E239K mutant, the positive charge in $\beta 7$ (K239 and the next K240) interacts with the negative charge of the neck domain (D363 and E362) (Figs 5C and 6E). Therefore, the stability of the docked conformation persists abnormally in the mutant (Fig 6A–D), and as a result, the structural change to the undocked conformation and the accompanying release of Pi and ADP can be delayed (Fig 4H). The extension of the transitional state of ATP hydrolysis means that KIF1A(E239K) tends to hold nucleotides in the motor domain for longer. Imbalance of the cell energy currency disrupts the essential function of the KIF1A motor that smoothly steps on the microtubule, which may delay the transport and cause the diseases.

The $\beta 7$ -neck interaction mediates the force flow of the motor domain

Based on the findings obtained thus far, it is expected that the interaction of $\beta 7$ E239 with the neck is related to the force flow throughout the motor domain. ATP binding, hydrolysis, and ADP release in the nucleotide-binding pocket produce twisting of the central β -sheet through the interaction of the P-loop with the microtubule-binding loop L11 (Gigant *et al*, 2013; Kull & Endow, 2013; Arora *et al*, 2014) with a large inclination at the plus-end tip of the central β -sheet (Shang *et al*, 2014). This links to the structural change in the microtubule interface helix $\alpha 4$ (Nitta *et al*, 2004; Hirose *et al*, 2006; Sindelar & Downing, 2010; Atherton *et al*, 2014), docking/undocking of the neck initial segment to the hydrophobic pocket of motor domain, and production of driving force by the neck-linker formation (Vale & Milligan, 2000). Structural studies (Kikkawa *et al*, 2001; Sablin & Fletterick, 2001, 2004) and simulated molecular dynamics studies (Hwang *et al*, 2008; Geng *et al*, 2014; Budaitis *et al*, 2021) both showed that the microtubule-binding domain ($\alpha 4$ and $\alpha 5$) and

the N-terminus end region dock with the initial segment of the neck-linker and position the neck domain to lie along the right side of the central β -sheet. Since $\beta 7$ E239 is located at the plus-end on the right side of the central β -sheet (Fig EV5), we speculate that residue E239 may have a role in propagating structural changes in the nucleotide-binding domain throughout the motor domain, via the twist of the central β -sheet and the interaction between the microtubule-binding region and the root of the neck-linker, leading to regulation of the neck domain.

Not only $\beta 7$ but also the nucleotide-binding region ($\alpha 1$ - $\beta 3$ -P loop) and microtubule-binding regions ($\alpha 4$ -L12 and L12- $\alpha 5$) showed unnecessarily strong intramolecular interactions in the E239K mutant in the ADP-ADP state (Appendix Fig S6). Additionally, in the structural comparison between the WT and mutant, the C α -C α RMSD in the nucleotide-binding region and neck-coil located on the left and right sides of the central β -sheet was large (Fig EV5). These results reinforce our model that $\beta 7$ mutation affects a series of allosteric rearrangements that connect the ATP hydrolysis center to the neck movement.

The fast and processive movement of kinesin-3 is associated with a relatively weak interaction between the unique short neck-linker and motor domain (Ren *et al*, 2018b). A previous single-molecule measurement study on pathogenic KIF1A mutations linked to neurodevelopmental disorders showed that the KIF1A mutations V8 M in $\beta 1$ and Y89D in $\beta 3$ impair the neck-linker docking and dramatically reduce the force production of kinesin (Budaitis *et al*, 2021). Similar to $\beta 1$ and $\beta 3$, $\beta 7$ is also located in the neck-linker peripheral region (Appendix Fig S7), suggesting that it is a crucial element for kinesin movement. Molecular dynamics simulations have suggested that $\beta 7$ in the motor domain interacts with the second half of the neck-linker (Budaitis *et al*, 2019). However, the previous study showed the conventional kinesin (KIF5C) mutants impairing the motor-neck “latch” interactions, but not enhancing them. These mutants paradoxically revealed a combination of increase in the motor velocity and decrease in the motor force output, but the mechanism remained elusive. In our study, we provided the new critical evidence that the neuropathogenic E239K mutant of KIF1A hyperstabilized the motor-neck interaction and thus reduced the motor velocity, possibly by impairing the smooth release of the neck from the motor domain upon ATP hydrolysis. These data will first answer why the motor-neck interaction “costs” to motor speed for mechanical force generation, from the compelling evidence that the dissociation phase of the motor-neck interaction also significantly matters for the kinesin motor cycle. Accordingly, this atomic-level characterization of neuropathogenic kinesin mutation provided mechanistic insights into the kinesin mechanocoupling cycle. It will be one of the first to describe the physiological relevance of the proper dissociation kinetics of $\beta 7$ -neck coupling, which will deeply serve for the multidisciplinary understanding of the kinesin-related neuropathies.

Materials and Methods

Subjects, exome sequencing analysis, standard protocol approvals, and patient consent

Two brothers were identified to have dominant CMT2. Clinical genetic testing of the MFN2 gene was performed and was negative.

Exome sequencing was performed to determine the genetic cause of the CMT2 at the University of Miami. Written informed consent was obtained from both subjects, and the study was approved by the institutional review board of the University of Iowa.

Mice

All animal procedures were approved by the University of Tokyo Institutional Animal Care and Use Committee and performed in accordance with the Guiding Principles for the Care and Use of Laboratory Animals. *Kif1a*^{+/-} mice have been described previously (Tanaka *et al*, 2016).

Primary culture of mouse DRG neurons

DRGs were obtained from 9- to 12-month-old male *Kif1a*^{+/+} and *Kif1a*^{+/-} mice according to a previously described method (Heinrich *et al*, 2016). Isolated DRGs were treated with 2.5 mg/ml of collagenase (Worthington) at 37°C for 1 h and then with 0.25% of trypsin at 37°C for 15 min. The cells were rinsed with medium A consisting of MEM (Gibco) with 33.3 mM of glucose (Wako), 1 mM of sodium pyruvate (Wako), 2 mM of GlutaMAX-I supplement (Gibco), and 10% fetal bovine serum (Cell Culture Bioscience) and centrifuged at 1,000 rpm for 10 min. The cells were then resuspended in medium B, which was prepared by adding 5 μM of Ara-C (Calbiochem), MACS NeuroBrew-21 (Miltenyi Biotec), 50 ng/ml of mouse 2.5S NGF (BD Biosciences) and antibiotics (penicillin-streptomycin; Thermo Fisher) to medium A. The cells were plated on an 8-well Lab-Tek II Chambered Coverglass (Thermo Scientific) precoated with 20 μg/ml of laminin (Sigma). The medium was changed after 18 h of incubation and maintained at 37°C in 5% CO₂.

Microfluidic chamber culture

A microfluidic chamber with 450-μm microchannels (Xona Microfluidics) was used for the compartmental culture of DRG neurons (Appendix Fig S1). The coverslips and microfluidic chambers were sterilized as described previously (Xu *et al*, 2018). The washed and dried cover glasses and microfluidic chambers were combined, coated with 20 μg/ml of laminine (Sigma) overnight, and preincubated with MEM (Gibco) containing 33.3 mM of glucose (Wako), 1 mM of sodium pyruvate (Wako), 2 mM of GlutaMAX-I supplement (Gibco), and 10% fetal bovine serum (Cell Culture Bioscience). Dissociated DRG neurons were loaded to the left main channel of the chamber in two drops of 10 μl each at a concentration of ~4 × 10⁶ cells/ml. After 5 min of incubation, the medium consisting of MEM with 33.3 mM of glucose, 1 mM of sodium pyruvate, 2 mM of GlutaMAX-I supplement, 10% fetal bovine serum, 5 μM of Ara-C (Calbiochem), MACS NeuroBrew-21 (Miltenyi Biotec), 50 ng/ml of mouse 2.5S NGF (BD Biosciences), and antibiotics (penicillin-streptomycin; Thermo Fisher) was introduced into the four channels of the chamber. The medium was changed after 18 h of incubation and maintained at 37°C in 5% CO₂.

Expression and knockdown vectors

The *KIF1A-EGFP* expression vector was generated by ligating full-length mouse *Kif1a* cDNA to *pEGFP-N1* (Clontech). To introduce the

c.715g>a mutation, the QuikChangeII XL kit (Agilent Technologies) was used with the following primer set: 5'-GATTTTGCTCAC TTTCTTTGTGGTGATGTTGGTCTCTGC-3' (sense) and 5'-GCAGAG ACCAACATCACCACAAAGAAAGTGAGCAAATC-3' (antisense). Adenovirus was generated using a ViraPower Adenoviral Expression System (Invitrogen/Thermo Fisher) and purified with CsCl centrifugation, as previously described (Yang *et al*, 2014). The *ECFP-TrkA* expression vector has been previously described (Tanaka *et al*, 2016). The *TagRFP-Rab3QL* and *TagRFP-synaptotagmin* expression vectors have also been previously described (Niwa *et al*, 2008). The TagRFP-tagged miRNA-based knockdown vector (KD1 vector, Mmi512592) for the mouse *Kif1a* gene and the scrambled control have been described previously (Tanaka *et al*, 2016). To introduce miRNA immune silent mutations and to generate adenovirus, the following primer set was used: 5'-GTCAGTTTCTGGGGTGTTC CGTATCCGTCGACTACTAGCTCGCGCACTTCC-3' (sense) and 5'-GGAAGTGC GCGAGCTAGTAGTCGGACGATAACGCAACACCCAGAACTGAC-3' (antisense).

Immunocytochemistry

DRG neurons isolated from 9- to 12-month-old *Kif1a*^{+/+} and *Kif1a*^{+/-} mice were transduced with adenoviral vectors encoding KIF1A-EGFP and KIF1A(E239K)-EGFP at DIV 5. Then, the cultures at DIV 7 were fixed with 4% PFA in PBS at 37°C for 10 min, permeabilized with 0.1% Triton X-100 in PBS at RT for 5 min, and blocked with 5% bovine serum albumin (BSA; Roche Diagnostics) in PBS at RT for 20 min. For staining the surface TrkA and surface TRPV1, the process of permeabilization was skipped. The neurons were then incubated with a primary antibody diluted in Can Get Signal immunostaining solution A (Toyobo) or blocking buffer at 4°C overnight and then incubated with an Alexa Fluor-conjugated secondary antibody diluted in blocking buffer at RT for 1 h. The stained DRG axons were observed under a confocal laser-scanning microscope (LSM780 with Airyscan; ZEISS) equipped with an alpha Plan-Apochromat oil-immersion objective lens (100×, NA 1.46; ZEISS). The images were statistically analyzed using Fiji. The density of the signal particles in the images was calculated for quantitative comparisons of surface TrkA, surface TRPV1, Rab3A, synaptotagmin, and DENN/MADD in 8-well chambers. For the control α-tubulin quantification, the fluorescence intensity was calculated instead of the signal density, since microtubules are dyed linearly.

Antibodies

The following antibodies were obtained and used for immunofluorescence experiments: anti-KIF1A antibody (RRID:AB_2314702) (Tanaka *et al*, 2016) diluted 1:500; anti-TrkA antibody (RRID: AB_10658910; #ANT-018; Alomone Labs) diluted 1:100; anti-TRPV1 antibody (RRID:AB_2040258; #ACC-029; Alomone Labs) diluted 1:1000; anti-Rab3A antibody (RRID: AB_632292; #sc-308; Santa Cruz Biotechnology) diluted 1:200; anti-synaptotagmin antibody (RRID:AB_2315417; #MAB5202; Millipore) diluted 1:1000; anti-DENN/MADD antibody (RRID:AB_260589; M5683; Sigma-Aldrich) diluted 1:500; anti-α-tubulin antibody DM1A (RRID: AB_477583; T6199; Sigma-Aldrich) diluted 1:10,000; and Alexa-Fluor-labeled IgGs (Thermo Fisher) diluted 1:500.

Live cell imaging

Cultured DRG neurons isolated from 10–12-month-old *Kif1a*^{+/+} and *Kif1a*^{+/-} mice were transduced with adenoviral vectors. Knock-down vectors were transduced at DIV 1, and KIF1A, TrkA, Rab3QL, synaptotagmin expression vectors described above were transduced at DIV 4–6. After 24–30 h of incubation, the DRG axons were observed using a confocal laser-scanning microscope (LSM780 with Airyscan; ZEISS) equipped with an alpha Plan-Apochromat oil-immersion objective lens (100 \times , NA 1.46; ZEISS). Images were captured continuously at 567 ms intervals for 250 frames. For mitochondrial imaging, the cells were labeled with MitoBright LT deep red (Dojindo) at DIV 13 and observed with a C-Apochromat lens (40 \times , NA 1.20; ZEISS). Data analyses and kymograph generation were performed using Fiji software. The velocity of the particles and their directions were calculated from the slope of the kymographs.

KIF1A constructs and tubulin preparation

The coding sequences of the mouse KIF1A aa 1–382 (KIF1A382), 1–400 (KIF1A400), 1–472 (KIF1A472), and their E239K mutants were cloned into pET21b (+) (Novagen) with a His₇-tag at the C-terminus. The constructs were transformed into *E. coli* strain BL21 (DE3) cells (Novagen). Protein expression was induced by the addition of 0.5 mM of IPTG to cultures followed by incubation at 22°C for 18 h. Immobilized metal affinity chromatography (TALON Metal Affinity Column; Clontech), cation exchange chromatography (AKTA pure, Resource S; Cytiva) and size exclusion chromatography (Superdex 200 Increase; Cytiva) were sequentially used for purification. The purified KIF1A proteins were concentrated, frozen in liquid N₂ and stored at –80°C. Tubulin was purified from porcine brains by six cycles of polymerization and depolymerization using high-molarity PIPES buffer (1 M PIPES-KOH, 1 mM of EGTA, and 1 mM of MgCl₂, pH 6.8) to remove contaminating microtubule-associated proteins (Castoldi & Popov, 2003). Purified tubulin was polymerized in PEM buffer (100 mM of PIPES-KOH, 1 mM of EGTA, 1 mM of MgCl₂, pH 6.8) containing 1 mM of GTP and 7% DMSO at 37°C for 30 min. For the microtubule gliding, ATPase, and mant-nucleotide assays, taxol was added in a stepwise fashion to a final concentration of 10 μ M. The labeled tubulin for the gliding assay was prepared by incubating the polymerized microtubule, which was obtained after four cycles of polymerization and depolymerization, with tetramethylrhodamine succinimidyl ester (C-1171; Life Technologies) for 30 min at 37°C (Desai & Mitchison, 1998). Then, functionally labeled tubulin was purified through two cycles of polymerization and depolymerization.

ATPase assay

The ATPase assay was performed as described previously (Wang et al, 2016) with slight modifications. Briefly, microtubule-stimulated ATPase kinetics of KIF1A WT and E239K were measured at 27°C with the EnzChek Phosphate Assay Kit (Molecular Probes) using a spectrophotometer (V630-Bio; JASCO). The absorbance at 360 nm was recorded every 2 s in PEM buffer containing 5-nM KIF1A (WT/E239K), 10 μ M of Taxol, 10 mM of Mg-ATP, and

varying concentrations of taxol-stabilized microtubules (0–10 μ M). The ATP hydrolysis rate was calculated from the slope of the absorbance plot and fit the Michaelis-Menten model.

Microtubule gliding assay

Microtubule gliding assays were performed as described previously with slight modifications (Morikawa et al, 2015). A flow chamber assembled from a glass slide and a coverslip was coated with a penta-His antibody (Qiagen) for 3 min and washed with casein-containing buffer (80-mM PIPES pH 6.8 adjusted with KOH, 1 mM of EGTA, 1 mM of MgCl₂, 1.25 mg/ml of casein, 10 mM of DTT, and 10 μ M of Taxol). After 3 min of incubation, 20 μ g/ml of motor protein was introduced to allow its immobilization at the C-terminal His-tag for 5 min. The chamber was then washed and blocked with the buffer. Subsequently, the microtubule solution was injected into the chamber together with the motility buffer (80 mM PIPES pH 6.8 adjusted with KOH, 1 mM of EGTA, 1 mM of MgCl₂, 1.25 mg/ml of casein, 5 mM of ATP, 10 μ M of Taxol and 20 mM of glucose) and an oxygen scavenging system consisting of 50 μ g/ml of glucose oxidase, 50 μ g/ml of catalase and 10 mM of DTT. Time-lapse images were acquired using the ELYRA P.1 system in TIRF mode at 37°C. The gliding velocity was calculated from the slope of the kymograph generated using the Fiji plugin Multi-kymograph (Rietdorf J and Seitz A, Available: http://fiji.sc/Multi_Kymograph).

Measurements of the mant-ATP association and dissociation, and the mant-ADP dissociation

The mant-ATP and mant-ADP assays were basically performed as described previously (Patel et al, 2014) with some modifications. To prepare nucleotide-free KIF1A for mant-ATP experiment, KIF1A (WT) and KIF1A(E239K) (aa 1–382) were mixed with 1 mM of EDTA and 1 mM of DTT in Mg-free buffer (80 mM of PIPES-KOH pH 6.9, 1 mM of EGTA and 0.1% Tween20). After 5 min incubation at 4°C, free nucleotides and EDTA were removed using NAP-5 Columns (17-0853-02; GE Healthcare). MgCl₂ was added in the collection tubes to a final concentration of 1 mM. Mant-ATP (M12417; Thermo fisher) was diluted to 5–50 μ M using reaction buffer (80-mM PIPES-KOH pH 6.9, 1 mM of EGTA, 1 mM of MgCl₂, and 0.1% Tween20). Nucleotide-free KIF1A solution (4 μ M) and mant-ATP solution (5–50 μ M) were set and mixed in a 1:1 v/v ratio using a spectrofluorometer (FP-8500; Jasco) equipped with a stopped-flow system (SFS-852T; Jasco) at 27°C. Excitation wavelength was at 365 nm and emissions at 440–500 nm was collected using a L42 filter at a measurement interval of 10 ms.

To prepare mant-ADP-KIF1A complex for mant-ADP experiment, 100 μ M of KIF1A(WT) and KIF1A(E239K) were mixed with 800 μ M mant-ADP (M12416; Thermo fisher) in the reaction buffer and incubated at 25°C for 20 min. Excess mant-ADP was removed using NAP-5 Columns. Then, mant-ADP-KIF1A complex solution (50 μ M) and unlabeled ATP solution (5 mM) were mixed using the stopped-flow fluorometer. For the measurement of the microtubule-stimulated mant-ADP dissociation, 4- μ M microtubules stabilized with 40 μ M of taxol were supplemented in unlabeled ATP solution. The fluorescence intensity data were analyzed and fitted by using the GraphPad Prism 9.

Analytical size exclusion chromatography for KIF1A fragments

The wild type and the E239K-mutated KIF1A fragments (aa 1–382, 1–400, and 1–472) were bacterially expressed and purified as described above. Each fragment was assayed on size exclusion chromatography (Superdex 200 Increase; Cytiva) with buffer (20 mM of PIPES-KOH pH 7.0, 150 mM of KCl, 1 mM of MgCl₂ and 0.1% Tween20). Standard globular proteins, including Ferritin, Aldolase, Ovalbumin, and Ribonuclease, were used to prepare the calibration curve to determine the Stokes radius (Rs). The void volume (V₀) was determined with blue dextran 2000 (Cytiva). K_{av} (the partition coefficient) of each standard protein was calculated from its retention volume. Calibration curve was prepared by plotting the K_{av} versus its corresponding log₁₀Rs value, and used to determine Rs of the KIF1A fragments.

X-ray crystallography of KIF1A WT and E329K with ADP-AlFx

For X-ray crystallography, ADP-AlFx was introduced by incubation with KIF1A (aa 1–382) and microtubules for 30 min at 27°C during purification. WT KIF1A and the E239K mutant were screened for crystallization by an automated large-scale protein crystallization and monitoring system (Hiraki *et al*, 2006). A crystal was obtained at 25% PEG3350, 0.1 M Bis-Tris pH 5.5, and 0.2 M ammonium acetate by the sitting-drop method. X-ray diffraction data were collected at the BL-41XU beamline at the Spring-8 and BL-5A beamlines of KEK-PF. Collected data were processed by using the HKL2000 software package (Otwinowski & Minor, 1997). The structures were determined by the molecular replacement method. Electron-density maps based on the 2Fo-Fc coefficients were calculated from the phases of the initial model. Subsequent rounds of model building and refinement were performed using the program COOT (Emsley *et al*, 2010) and the CCP4 package (Winn *et al*, 2011), respectively. The WT KIF1A model was refined to R and R_{free} values of 22.8 and 23.7%, respectively (30.0–2.57 Å). The E239K mutant structure was similarly determined and refined to R and R_{free} values of 21.5 and 24.0%, respectively (30.0–1.76 Å). Details of the data collection and refinement are presented in Table 3.

Quantitative analysis of motor-neck interaction by the combination of protein Painting and stable isotope tag labeling

The coupling reaction of Fast Blue B (D9805; Sigma) salt and an excess of naphthionic acid (250619; Sigma) (3-fold molar concentration to FBB) was conducted in Dulbecco's PBS at room temperature as reported previously (Haymond 2019). The binding assay was performed in BRB80 buffer containing 5 nM KIF1A382 (WT or E239K) and taxol-stabilized polymerized microtubules (5 nM as tubulin dimer) in the absence/presence of unhydrolysable ATP analogues (ADP-BeFx and ADP-AlFx) for 15 min at 27°C. The assay mixtures were mixed with FBB dye at a 100-fold molar ratio of dye to protein. After the painting reaction was allowed to proceed for 5 min, the dye/protein mixtures were quickly passed through MicroSpin G-25 columns (27-5325-01; Cytiva) at 4°C with buffer containing 500 mM of KCl to remove unbound dye. Painted mixtures were reduced, alkylated, and digested into peptides. In tryptic digestion, the paints inhibit digestion, allowing the protein–protein interaction sites to be mapped by mass spectrometry (Luchini *et al*,

2014; Haymond *et al*, 2019). For quantitation of mapping sites, each peptide solution was labeled with differential stable isotope TMT Reagents 126-131 (Thermo Scientific): 126 (WT), 127 (WT + ADP-BeFx), 128 (WT + ADP-AlFx), 129 (E239K), 130 (E239K + ADP-BeFx), and 131 (E239K + ADP-AlFx). After quenching of the reaction and removal of the extra labeling dyes, the samples were combined and quantitatively analyzed using tandem mass spectrometry on an LTQ-Orbitrap Velos with an Easy-nLC system (Thermo Scientific). The peptide mixtures were separated using a gradient from 5 to 45% CAN in 45 min with a flow rate of 600 nl/min. The data were searched against the NCBI and SWISS-PROT databases and obtained in-house for the recombinant wild-type and mutant KIF1A proteins using SEQUEST (Thermo Scientific) and MASCOT (Matrix Science) in Proteome Discoverer 2.4 (Thermo Scientific). Two missed cleavages were allowed for each peptide, with a maximum mass of 5,000 Da. The precursor ion tolerance was set to 5 ppm for HCD and 0.7 Da for CID. The data were searched, allowing oxidation (M) and TMT6plex (N-terminal, K) as a variable modification and carbamidomethylation (C) as a fixed modification. The MS/MS fragments were simultaneously used to assign the fragments of protein–protein interaction sites and to quantify the relative level of each peptide by the intensities of the unique reporter ions from the TMT-tags.

Data availability

Coordinates for KIF1A structures have been deposited in the PDB and are available under the accession codes 7EOB (KIF1A E239K: ADP-AlFx; <https://www.rcsb.org/structure/7EOB>) and 7EO9 (KIF1A WT:ADP-AlFx; <https://www.rcsb.org/structure/7EO9>). The MS raw data and analysis files have been deposited in the ProteomeXchange Consortium via jPOST under the dataset identifiers “jPOST: JPST001177” and “ProteomeXchange:PXID026083” (<http://proteomecentral.proteomexchange.org/cgi/GetDataset?ID=PXID026083>).

Expanded View for this article is available online.

Acknowledgments

The authors thank Dr. K. Hasegawa and all the staff of Spring-8 as well as Drs. T. Senda, N. Matsugaki, Y. Yamada, M. Senda, and all the staff of the Photon Factory for help with X-ray crystal data collection; H. Souda, T. Uchiyama, A. Yamane (Jasco corporation) for setting up and acquiring data for the mantle nucleotide experiments using a stopped-flow spectrofluorometer (FP-8500 and SFS-852T; Jasco); T. Akamatsu, N. Onouchi, I. Takemura, H. Koike, Y. Miyamoto, H. Sato, H. Fukuda, and all the members of the N.H. laboratory for their technical help and valuable discussions. This work was supported by grants from the Japan Society for the Promotion of Science (JSPS) KAKENHI (grant numbers JP23000013 and JP16H06372) to N.H., from the Japan Agency for Medical Research and Development (AMED) Strategic Research Program for Brain Sciences (grant number JP20dm0107084) to N.H. and Y.T., and from the Uehara Memorial Foundation to N.H. and by a JSPS Grant-in-Aid for Early-Career Scientists (grant number JP20K16483) to Ma.M. X-ray crystallography experiments were performed at beamline BL41XU of Spring-8 with the approval of the Japan Synchrotron Radiation Research Institute (JASRI) (Proposal No. 2017A2539 and 2018A2552) and supported by the Platform Project for Supporting Drug Discovery and Life Science Research (Basis for Supporting Innovative Drug Discovery and Life Science Research (BINDS)) from AMED

under Grant Number JP20am0101070 (support number 1487). X-ray crystallography experiments were also performed at beamline BL-5A of KEK-PF under the approval of the Photon Factory Program Advisory Committee (Proposal No. 2018G143) and supported by BINDS from AMED under Grant Number JP20am0101071 (support number 1133). The work was also supported by grants from the National Institute of Neurological Disorders and Stroke (M.E.S.), the Office of Rare Diseases (M.E.S., U54NS065712), the Muscular Dystrophy Association (M.E.S.), and the Charcot-Marie-Tooth Association (M.E.S.) and by a Muscular Dystrophy Association Clinical Research Training grant (N.U.).

Author contributions

Nobutaka Hirokawa: Conceptualization; Supervision; Funding acquisition; Project administration; Writing—review & editing. **Manatsu Morikawa:** Conceptualization; Data curation; Formal analysis; Funding acquisition; Validation; Investigation; Visualization; Writing—original draft. **Nivedita U Jerath:** Conceptualization; Data curation; Funding acquisition; Investigation; Writing—review & editing. **Tadayuki Ogawa:** Formal analysis; Investigation; Methodology; Writing—review & editing. **Momo Morikawa:** Data curation; Formal analysis; Investigation; Visualization; Writing—review & editing. **Yosuke Tanaka:** Supervision; Methodology; Writing—review & editing. **Michael E Shy:** Funding acquisition; Writing—review & editing. **Stephan Züchner:** Data curation; Formal analysis; Supervision; Funding acquisition; Writing—review & editing.

In addition to the CRediT author contributions listed above, the contributions in detail are:

NH conceived and directed the project. NUJ, MES, and SZ performed the clinical studies. MaM, MoM, and YT performed the cell biology experiments. TO and MaM performed the biochemical and biophysical experiments. MaM, TO, MoM, YT, and NH discussed the data and wrote the manuscript.

Disclosure and competing interests statement

The authors declare that they have no conflict of interest.

References

- Arora K, Talje L, Asenjo AB, Andersen P, Atchia K, Joshi M, Sosa H, Allingham JS, Kwok BH (2014) KIF14 binds tightly to microtubules and adopts a rigor-like conformation. *J Mol Biol* 426: 2997–3015
- Atherton J, Farabella I, Yu IM, Rosenfeld SS, Houdusse A, Topf M, Moores CA (2014) Conserved mechanisms of microtubule-stimulated ADP release, ATP binding, and force generation in transport kinesins. *eLife* 3: e03680
- Auerbach SD, Johnson KA (2005) Kinetic effects of kinesin switch I and switch II mutations. *J Biol Chem* 280: 37061–37068
- Brendza KM, Sontag CA, Saxton WM, Gilbert SP (2000) A kinesin mutation that uncouples motor domains and desensitizes the gamma-phosphate sensor. *J Biol Chem* 275: 22187–22195
- Bucci C, Bakke O, Progida C (2012) Charcot-Marie-Tooth disease and intracellular traffic. *Prog Neurobiol* 99: 191–225
- Budaitis BG, Jariwala S, Reinemann DN, Schimert KI, Scarabelli G, Grant BJ, Sept D, Lang MJ, Verhey KJ (2019) Neck linker docking is critical for kinesin-1 force generation in cells but at a cost to motor speed and processivity. *eLife* 8: 1–28
- Budaitis BG, Jariwala S, Rao L, Yue Y, Sept D, Verhey KJ, Gennerich A (2021) Pathogenic mutations in the kinesin-3 motor KIF1A diminish force generation and movement through allosteric mechanisms. *J Cell Biol* 220: e202004227
- Cao L, Wang W, Jiang Q, Wang C, Knossow M, Gigant B (2014) The structure of apo-kinesin bound to tubulin links the nucleotide cycle to movement. *Nat Commun* 5: 5364
- Case RB, Rice S, Hart CL, Ly B, Vale RD (2000) Role of the kinesin neck linker and catalytic core in microtubule-based motility. *Curr Biol* 10: 157–160
- Castoldi M, Popov AV (2003) Purification of brain tubulin through two cycles of polymerization-depolymerization in a high-molarity buffer. *Protein Expr Purif* 32: 83–88
- Cheon CK, Lim SH, Kim YM, Kim D, Lee NY, Yoon TS, Kim NS, Kim E, Lee JR (2017) Autosomal dominant transmission of complicated hereditary spastic paraplegia due to a dominant negative mutation of KIF1A, SPG30 gene. *Sci Rep* 7: 1–11
- Chiba K, Takahashi H, Chen M, Obinata H, Arai S, Hashimoto K, Oda T, McKenney RJ, Niwa S (2019) Disease-associated mutations hyperactivate KIF1A motility and anterograde axonal transport of synaptic vesicle precursors. *Proc Natl Acad Sci U S A* 116: 18429–18434
- Cross RA (2016) Review: mechanochemistry of the kinesin-1 ATPase. *Biopolymers* 105: 476–482
- Desai A, Mitchison TJ (1998) Preparation and characterization of caged fluorescein tubulin. *Methods Enzymol* 298: 125–132
- Ekins S, Litterman NK, Arnold RJG, Burgess RW, Freundlich JS, Gray SJ, Higgins JJ, Langley B, Willis DE, Notterpek L et al (2015) A brief review of recent Charcot-Marie-Tooth research and priorities. *F1000Research* 4: 1–15
- Emsley P, Lohkamp B, Scott WG, Cowtan K (2010) Features and development of Coot. *Acta Crystallogr Sect D Biol Crystallogr* 66: 486–501
- Endow SA, Higuchi H (2000) A mutant of the motor protein kinesin that moves in both directions on microtubules. *Nature* 406: 913–916
- Esmaeli Nieh S, Madou MRZ, Sirajuddin M, Fregeau B, McKnight D, Lexa K, Strober J, Spaeth C, Hallinan BE, Smaoui N et al (2015) De novo mutations in KIF1A cause progressive encephalopathy and brain atrophy. *Ann Clin Transl Neurol* 2: 623–635
- Fisher AJ, Smith CA, Thoden JB, Smith R, Sutoh K, Holden HM, Rayment I (1995) X-ray structures of the myosin motor domain of Dictyostelium discoideum complexed with MgADP.BefX and MgADP.AIF4-. *Biochemistry* 34: 8960–8972
- Geng Y-Z, Liu S-X, Ji Q, Yan S (2014) Mechanical amplification mechanism of kinesin's β -domain. *Arch Biochem Biophys* 543: 10–14
- Gigant B, Wang W, Dreier B, Jiang Q, Pecqueur L, Plückthun A, Wang C, Knossow M (2013) Structure of a kinesin-tubulin complex and implications for kinesin motility. *Nat Struct Mol Biol* 20: 1001–1007
- Hall DH, Hedgecock EM (1991) Kinesin-related gene unc-104 is required for axonal transport of synaptic vesicles in *C. elegans*. *Cell* 65: 837–847
- Hancock WO (2016) The Kinesin-1 Chemomechanical Cycle: stepping toward a consensus. *Biophys J* 110: 1216–1225
- Haymond A, Dey D, Carter R, Dailing A, Nara V, Nara P, Venkatayogi S, Paige M, Liotta L, Luchini A (2019) Protein painting, an optimized MS-based technique, reveals functionally relevant interfaces of the PD-1/PD-L1 complex and the YAP2/ZO-1 complex. *J Biol Chem* 294: 11180–11198
- Heinrich T, Hübner CA, Kurth I (2016) Isolation and primary cell culture of mouse dorsal root ganglion neurons. *Bio-protocol* 6: e1785
- Hiraki M, Kato R, Nagai M, Satoh T, Hirano S, Ihara K, Kudo N, Nagae M, Kobayashi M, Inoue M et al (2006) Development of an automated large-scale protein-crystallization and monitoring system for high-throughput protein-structure analyses. *Acta Crystallogr Sect D Biol Crystallogr* 62: 1058–1065

- Hirokawa N (1998) Kinesin and dynein superfamily proteins and the mechanism of organelle transport. *Science* 279: 519–526
- Hirokawa N, Nitta R, Okada Y (2009a) The mechanisms of kinesin motor motility: lessons from the monomeric motor KIF1A. *Nat Rev Mol Cell Biol* 10: 877–884
- Hirokawa N, Noda Y, Tanaka Y, Niwa S (2009b) Kinesin superfamily motor proteins and intracellular transport. *Nat Rev Mol Cell Biol* 10: 682–696
- Hirose K, Akimaru E, Akiba T, Endow SA, Amos LA (2006) Large conformational changes in a kinesin motor catalyzed by interaction with microtubules. *Mol Cell* 23: 913–923
- Howard J, Hudspeth AJ, Vale RD (1989) Movement of microtubules by single kinesin molecules. *Nature* 342: 154–158
- Hua W, Young EC, Fleming ML, Gelles J (1997) Coupling of kinesin steps to ATP hydrolysis. *Nature* 388: 390–393
- Hwang W, Lang MJ, Karplus M (2008) Force generation in kinesin hinges on cover-neck bundle formation. *Structure* 16: 62–71
- Jennings S, Chenevert M, Liu L, Mottamal M, Wojcik EJ, Huckaba TM (2017) Characterization of kinesin switch I mutations that cause hereditary spastic paraplegia. *PLoS One* 12: 1–19
- Kikkawa M, Sablin EP, Okada Y, Yajima H, Fletterick RJ, Hirokawa N (2001) Switch-based mechanism of kinesin motors. *Nature* 411: 439–445
- Klebe S, Lossos A, Azzedine H, Mundwiler E, Sheffer R, Gausson M, Marelli C, Nawara M, Carpentier W, Meyer V et al (2012) KIF1A missense mutations in SPG30, an autosomal recessive spastic paraplegia: distinct phenotypes according to the nature of the mutations. *Eur J Hum Genet* 20: 645–649
- Klumpp LM, Brendza KM, Rosenberg JM, Hoenger A, Gilbert SP (2003) Motor domain mutation traps kinesin as a microtubule rigor complex. *Biochemistry* 42: 2595–2606
- Kull FJ, Endow SA (2013) Force generation by kinesin and myosin cytoskeletal motor proteins. *J Cell Sci* 126: 9–19
- Lawrence CJ, Dawe RK, Christie KR, Cleveland DW, Dawson SC, Endow SA, Goldstein LSB, Goodson HV, Hirokawa N, Howard J et al (2004) A standardized kinesin nomenclature. *J Cell Biol* 167: 19–22
- Lee J-R, Srour M, Kim D, Hamdan FF, Lim S-H, Brunel-Guitton C, Décarie J-C, Rossignol E, Mitchell GA, Schreiber A et al (2015) *De novo* mutations in the motor domain of KIF1A cause cognitive impairment, spastic paraparesis, axonal neuropathy, and cerebellar atrophy. *Hum Mutat* 36: 69–78
- Liu H-L, Pemble 4th CW, Endow SA (2012) Neck-motor interactions trigger rotation of the kinesin stalk. *Sci Rep* 2: 236
- Luchini A, Espina V, Liotta LA (2014) Protein painting reveals solvent-excluded drug targets hidden within native protein-protein interfaces. *Nat Commun* 5: 4413
- Miki H, Setou M, Kaneshiro K, Hirokawa N (2001) All kinesin superfamily protein, KIF, genes in mouse and human. *Proc Natl Acad Sci U S A* 98: 7004–7011
- Morikawa M, Yajima H, Nitta R, Inoue S, Ogura T, Sato C, Hirokawa N (2015) X-ray and Cryo-EM structures reveal mutual conformational changes of kinesin and GTP-state microtubules upon binding. *EMBO J* 34: 1270–1286
- Murphy SM, Herrmann DN, McDermott MP, Scherer SS, Shy ME, Reilly MM, Pareyson D (2011) Reliability of the CMT neuropathy score (second version) in Charcot-Marie-Tooth disease. *J Peripher Nerv Syst* 16: 191–198
- Nitta R, Kikkawa M, Okada Y, Hirokawa N (2004) KIF1A alternately uses two loops to bind microtubules. *Science* 305: 678–683
- Niwa S, Tanaka Y, Hirokawa N (2008) KIF1B β - and KIF1A-mediated axonal transport of presynaptic regulator Rab3 occurs in a GTP-dependent manner through DENN/MADD. *Nat Cell Biol* 10: 1269–1279
- Ogawa T, Hirokawa N (2015) Microtubule destabilizer KIF2A undergoes distinct site-specific phosphorylation cascades that differentially affect neuronal morphogenesis. *Cell Rep* 12: 1774–1788
- Ogawa T, Saijo S, Shimizu N, Jiang X, Hirokawa N (2017) Mechanism of catalytic microtubule depolymerization via KIF2-tubulin transitional conformation. *Cell Rep* 20: 2626–2638
- Ohba C, Haginoya K, Osaka H, Kubota K, Ishiyama A, Hiraide T, Komaki H, Sasaki M, Miyatake S, Nakashima M et al (2015) *De novo* KIF1A mutations cause intellectual deficit, cerebellar atrophy, lower limb spasticity and visual disturbance. *J Hum Genet* 60: 739–742
- Okada Y, Yamazaki H, Sekine-Aizawa Y, Hirokawa N (1995) The neuron-specific kinesin superfamily protein KIF1A is a unique monomeric motor for anterograde axonal transport of synaptic vesicle precursors. *Cell* 81: 769–780
- Othmane KB, Middleton LT, Loprest LJ, Wilkinson KM, Lennon F, Rozear MP, Stajich JU, Gaskell PC, Roses AD, Pericak-Vance MA et al (1993) Localization of a gene (CMT2A) for autosomal dominant Charcot-Marie-Tooth disease type 2 to chromosome 1p and evidence of genetic heterogeneity. *Genomics* 17: 370–375
- Otwinowski Z, Minor W (1997) Processing of X-ray diffraction data collected in oscillation mode. *Methods Enzymol* 276: 307–326
- Patel JT, Belsham HR, Rathbone AJ, Friel CT (2014) Use of stopped-flow fluorescence and labeled nucleotides to analyze the ATP turnover cycle of kinesins. *J Vis Exp* 92: 1–6
- Pennings M, Schouten MI, van Gaalen J, Meijer RPP, de Bot ST, Kriek M, Saris CGJ, van den Berg LH, van Es MA, Zuidgeest DMH et al (2020) KIF1A variants are a frequent cause of autosomal dominant hereditary spastic paraplegia. *Eur J Hum Genet* 28: 40–49
- Ren J, Wang S, Chen H, Wang W, Huo L, Feng W (2018a) Coiled-coil 1-mediated fastening of the neck and motor domains for kinesin-3 autoinhibition. *Proc Natl Acad Sci U S A* 115: E11933–E11942
- Ren J, Zhang Y, Wang S, Huo L, Lou J, Feng W (2018b) Structural delineation of the neck linker of kinesin-3 for processive movement. *J Mol Biol* 430: 2030–2041
- Rice S, Lin AW, Safer D, Hart CL, Naber N, Carragher BO, Cain SM, Pechatnikova E, Wilson-Kubalek EM, Whittaker M et al (1999) A structural change in the kinesin motor protein that drives motility. *Nature* 402: 778–784
- Rivière J-B, Ramalingam S, Lavastre V, Shekarabi M, Holbert S, Lafontaine J, Srour M, Merner N, Rochefort D, Hince P et al (2011) KIF1A, an axonal transporter of synaptic vesicles, is mutated in hereditary sensory and autonomic neuropathy type 2. *Am J Hum Genet* 89: 219–230
- Roda RH, Schindler AB, Blackstone C (2017) Multigeneration family with dominant SPG30 hereditary spastic paraplegia. *Ann Clin Transl Neurol* 4: 821–824
- Sablin EP, Fletterick RJ (2001) Nucleotide switches in molecular motors: structural analysis of kinesins and myosins. *Curr Opin Struct Biol* 11: 716–724
- Sablin EP, Fletterick RJ (2004) Coordination between motor domains in processive kinesins. *J Biol Chem* 279: 15707–15710
- Sack S, Müller J, Marx A, Thormählen M, Mandelkow EM, Brady ST, Mandelkow E (1997) X-ray structure of motor and neck domains from rat brain kinesin. *Biochemistry* 36: 16155–16165
- Scarabelli G, Grant BJ (2013) Mapping the structural and dynamical features of kinesin motor domains. *PLoS Comput Biol* 9: e1003329
- Schnitzer MJ, Block SM (1997) Kinesin hydrolyses one ATP per 8-nm step. *Nature* 388: 386–390
- Shang Z, Zhou K, Xu C, Csencsits R, Cochran JC, Sindelar CV (2014) High-resolution structures of kinesin on microtubules provide a basis for nucleotide-gated force generation. *Elife* 3: e04686

- Shimizu T, Thorn KS, Ruby A, Vale RD (2000) ATPase kinetic characterization and single molecule behavior of mutant human kinesin motors defective in microtubule-based motility. *Biochemistry* 39: 5265–5273
- Sindelar CV (2011) A seesaw model for intermolecular gating in the kinesin motor protein. *Biophys Rev* 3: 85–100
- Sindelar CV, Budny MJ, Rice S, Naber N, Fletterick R, Cooke R (2002) Two conformations in the human kinesin power stroke defined by X-ray crystallography and EPR spectroscopy. *Nat Struct Biol* 9: 844–848
- Sindelar CV, Downing KH (2010) An atomic-level mechanism for activation of the kinesin molecular motors. *Proc Natl Acad Sci U S A* 107: 4111–4116
- Skre H (1974) Genetic and clinical aspects of Charcot-Marie-Tooth's disease. *Clin Genet* 6: 98–118
- Tanaka Y, Hirokawa N (2002) Mouse models of Charcot-Marie-Tooth disease. *Trends Genet* 18: S39–S44
- Tanaka Y, Kanai Y, Okada Y, Nonaka S, Takeda S, Harada A, Hirokawa N (1998) Targeted disruption of mouse conventional kinesin heavy chain, kif5B, results in abnormal perinuclear clustering of mitochondria. *Cell* 93: 1147–1158
- Tanaka Y, Niwa S, Dong M, Farkhondeh A, Wang L, Zhou R, Hirokawa N (2016) The molecular motor KIF1A transports the TrkA neurotrophin receptor and is essential for sensory neuron survival and function. *Neuron* 90: 1215–1229
- Timmerman V, Strickland AV, Züchner S (2014) Genetics of Charcot-Marie-Tooth (CMT) disease within the frame of the human genome project success. *Genes* 5: 13–32
- Tomishige M, Stuurman N, Vale RD (2006) Single-molecule observations of neck linker conformational changes in the kinesin motor protein. *Nat Struct Mol Biol* 13: 887–894
- Tripet B, Vale RD, Hodges RS (1997) Demonstration of coiled-coil interactions within the kinesin neck region using synthetic peptides. Implications for motor activity. *J Biol Chem* 272: 8946–8956
- Uchimura S, Oguchi Y, Hachikubo Y, Ishiwata S, Muto E (2010) Key residues on microtubule responsible for activation of kinesin ATPase. *EMBO J* 29: 1167–1175
- Vale RD, Milligan RA (2000) The way things move: looking under the hood of molecular motor proteins. *Science* 288: 88–95
- Verhoeven K, Claeys KG, Züchner S, Schröder JM, Weis J, Ceuterick C, Jordanova A, Nelis E, De Vriendt E, Van Hul M et al (2006) MFN2 mutation distribution and genotype/phenotype correlation in Charcot-Marie-Tooth type 2. *Brain* 129: 2093–2102
- Wang D, Nitta R, Morikawa M, Yajima H, Inoue S, Shigematsu H, Kikkawa M, Hirokawa N (2016) Motility and microtubule depolymerization mechanisms of the Kinesin-8 motor, KIF19A. *Elife* 5: 1–24
- Winn MD, Ballard CC, Cowtan KD, Dodson EJ, Emsley P, Evans PR, Keegan RM, Krissinel EB, Leslie AGW, McCoy A et al (2011) Overview of the CCP4 suite and current developments. *Acta Crystallogr Sect D Biol Crystallogr* 67: 235–242
- Woehlke G, Ruby AK, Hart CL, Ly B, Hom-Booher N, Vale RD (1997) Microtubule interaction site of the kinesin motor. *Cell* 90: 207–216
- Wordeman L (2003) Breathing down the neck of Unc104. *J Cell Biol* 163: 693–695
- Xu F, Takahashi H, Tanaka Y, Ichinose S, Niwa S, Wicklund MP, Hirokawa N (2018) KIF1B β mutations detected in hereditary neuropathy impair IGF1R transport and axon growth. *J Cell Biol* 217: 3480–3496
- Yajima H, Ogura T, Nitta R, Okada Y, Sato C, Hirokawa N (2012) Conformational changes in tubulin in GMPCPP and GDP-taxol microtubules observed by cryoelectron microscopy. *J Cell Biol* 198: 315–322
- Yamagishi M, Shigematsu H, Yokoyama T, Kikkawa M, Sugawa M, Aoki M, Shirouzu M, Yajima J, Nitta R (2016) Structural basis of backwards motion in Kinesin-1-Kinesin-14 chimera: implication for Kinesin-14 motility. *Structure* 24: 1322–1334
- Yang W, Tanaka Y, Bundo M, Hirokawa N (2014) Antioxidant signaling involving the microtubule motor KIF12 is an intracellular target of nutrition excess in beta cells. *Dev Cell* 31: 202–214
- Yildiz A, Tomishige M, Gennerich A, Vale RD (2008) Intramolecular strain coordinates kinesin stepping behavior along microtubules. *Cell* 134: 1030–1041
- Ylikallio E, Kim D, Isohanni P, Auranen M, Kim E, Lönnqvist T, Tynnismaa H (2015) Dominant transmission of de novo KIF1A motor domain variant underlying pure spastic paraplegia. *Eur J Hum Genet* 23: 1427–1430
- Yonekawa V, Harada A, Okada Y, Funakoshi T, Kanai Y, Takei Y, Terada S, Noda T, Hirokawa N (1998) Defect in synaptic vesicle precursor transport and neuronal cell death in KIF1A motor protein-deficient mice. *J Cell Biol* 141: 431–441
- Zhao C, Takita J, Tanaka Y, Setou M, Nakagawa T, Takeda S, Yang HW, Terada S, Nakata T, Takei Y et al (2001) Charcot-Marie-Tooth Disease Type 2A Caused by Mutation in a Microtubule Motor KIF1B β . *Cell* 105: 587–597